Faculty and Researchers | Faculty and Researchers' Publications

2015

Ekman spiral in horizontally inhomogeneous ocean with varying eddy viscosity

Chu, Peter C.

Springer

Ekman Spiral in Horizontally Inhomogeneous Ocean with Varying Eddy Viscosity

Peter C. Chu

Naval Ocean Analysis and Prediction Laboratory, Department of Oceanography

Naval Postgraduate School, Monterey, California, USA

Report Documentation Page		

Public reporting burden for the collection of information is estimated to average 1 hour per response, including the time for reviewing instructions, searching existing data sources, gathering and maintaining the data needed, and completing and reviewing the collection of information. Send comments regarding this burden estimate or any other aspect of this collection of information, including suggestions for reducing this burden, to Washington Headquarters Services, Directorate for Information Operations and Reports, 1215 Jefferson Davis Highway, Suite 1204, Arlington VA 22202-4302. Respondents should be aware that notwithstanding any other provision of law, no person shall be subject to a penalty for failing to comply with a collection of information if it does not display a currently valid OMB control number.

1. REPORT DATE **2015**	2. REPORT TYPE	3. DATES COVERED **00-00-2015 to 00-00-2015**

4. TITLE AND SUBTITLE **Ekman Spiral in Horizontally Inhomogeneous Ocean with Varying Eddy Viscosity**	5a. CONTRACT NUMBER
	5b. GRANT NUMBER
	5c. PROGRAM ELEMENT NUMBER
6. AUTHOR(S)	5d. PROJECT NUMBER
	5e. TASK NUMBER
	5f. WORK UNIT NUMBER

7. PERFORMING ORGANIZATION NAME(S) AND ADDRESS(ES) **Naval Postgraduate School,Naval Ocean Analysis and Prediction Laboratory,Monterey,CA,93943**	8. PERFORMING ORGANIZATION REPORT NUMBER

9. SPONSORING/MONITORING AGENCY NAME(S) AND ADDRESS(ES)	10. SPONSOR/MONITOR'S ACRONYM(S)
	11. SPONSOR/MONITOR'S REPORT NUMBER(S)

12. DISTRIBUTION/AVAILABILITY STATEMENT
Approved for public release; distribution unlimited

13. SUPPLEMENTARY NOTES
Pure and Applied Geophysics, 172, DOI 10.1007/s00024-015-1063-4.

14. ABSTRACT
Classical Ekman spiral is generated by surface wind stress with constant eddy viscosity in homogeneous ocean. In real oceans, the eddy viscosity varies due to turbulent mixing caused by surface wind and buoyancy forcing. Horizontally inhomogeneous density produces vertical geostrophic shear which contributes to current shear that also affects the Ekman spiral. Based on the similar theoretical framework as the classical Ekman spiral, the baroclinic components of the Ekman spiral caused by the horizontally inhomogeneous density are obtained analytically with the varying eddy viscosity calculated from surface wind and buoyancy forcing using the KProfile Parameterization (KPP). Along with the three existing types of eddy viscosity due to pure wind forcing (zero surface buoyancy flux), such an effect is evaluated using the climatological monthly mean data of surface wind stress, buoyancy flux, ocean temperature and salinity, and mixed layer depth.

15. SUBJECT TERMS

16. SECURITY CLASSIFICATION OF:			17. LIMITATION OF ABSTRACT	18. NUMBER OF PAGES	19a. NAME OF RESPONSIBLE PERSON
a. REPORT **unclassified**	b. ABSTRACT **unclassified**	c. THIS PAGE **unclassified**	**Same as Report (SAR)**	**54**	

Abstract

Classical Ekman spiral is generated by surface wind stress with constant eddy viscosity in homogeneous ocean. In real oceans, the eddy viscosity varies due to turbulent mixing caused by surface wind and buoyancy forcing. Horizontally inhomogeneous density produces vertical geostrophic shear which contributes to current shear that also affects the Ekman spiral. Based on the similar theoretical framework as the classical Ekman spiral, the baroclinic components of the Ekman spiral caused by the horizontally inhomogeneous density are obtained analytically with the varying eddy viscosity calculated from surface wind and buoyancy forcing using the K-Profile Parameterization (KPP). Along with the three existing types of eddy viscosity due to pure wind forcing (zero surface buoyancy flux), such an effect is evaluated using the climatological monthly mean data of surface wind stress, buoyancy flux, ocean temperature and salinity, and mixed layer depth.

1. Introduction

On the base of homogeneous density without considering waves, Ekman (1905) modeled turbulent mixing in upper ocean as a diffusion process similar to molecular diffusion, with an eddy viscosity (turbulent plus molecular), $\hat{K}$ (the symbol '^' indicating dimensional quantity), which was taken as a constant with many orders of magnitude larger than the molecular viscosity. The turbulent mixing generates ageostrophic component of the upper ocean currents (called the Ekman spiral), decaying by an e-folding over a depth as the current vector rotate to the right (left) in the northern (southern) hemisphere through one radian. Several approaches may advance the classical Ekman theory: (a) replacing constant eddy viscosity by varying eddy viscosity, and relating the eddy viscosity to ocean mixing (under surface wind and/or buoyancy forcing), (b) including ocean wave effect, and (c) changing homogeneous to inhomogeneous density.

It was recognized that the eddy viscosity $\hat{K}$ is not a constant. After fitting observational ocean currents to the Ekman spiral (e.g., Hunkins 1966; Stacey et al. 1986; Price et al. 1987; Richman et al. 1987; Chereskin 1995; Lenn and Chereskin 2009), the inferred $\hat{K}$ value varies more than an order of magnitude, from 0.054 m^2 s^{-1} (Price et al. 1987) obtained from the field measurements acquired from a surface mooring set in the western Sargasso Sea (34°N, 70°W) as part of the Long Term Upper Ocean Study Phase 3 (LOTUS-3) during the summer of 1982, to 0.006 m^2 s^{-1} (Stacey et al. 1986) obtained from the low-frequency current measurements in the Strait of Georgia, British Columbia. The smaller value (0.006 m^2 s^{-1}) may be treated as a lower bound of the eddy viscosity (Price et al. 1987). Recently, Lenn and Chereskin (2009) obtained a mean Ekman spiral from high-resolution repeat observations of upper-ocean velocity in Drake Passage along with the constant temperature in the Ekman layer (implying near neutral

stratification). The eddy viscosities inferred from Ekman theory and the time-averaged stress was directly estimated as $O(10^{-2}–10^{-1})$ m^2 s^{-1}.

The turbulent mixing in upper-ocean is also viewed as being driven by the atmospheric fluxes of momentum and buoyancy (heat and moisture), and the shear imposed by the ocean circulation, and characterized by the existence of a vertically quasi-uniform layer of temperature and density (i.e., mixed layer). Underneath the mixed layer, there exists another layer with a strong vertical gradient, such as the thermocline (in temperature) and pycnocline (in density) (e.g., Kraus and Turner 1967; Garwood 1977; Chu and Garwood 1991; Steger et al. 1998; Chu et al. 2002). Such vertical mixing generates varying upper-ocean eddy viscosity. The mixed layer is a key component in studies of climate and the link between the atmosphere and deep-ocean and directly affects the air–sea exchange of heat, momentum, and moisture (Chu 1993).

Effect of vertical inhomogeneity of density on the Ekman spiral (i.e., stratified Ekman layers) has been identified by observational and modeling studies in atmospheric boundary layer (Lettau and Dabberdt 1970; Grachev et al. 2008) and oceanic boundary layer (McWilliams et al. 2009; Taylor and Sarkar 2008). Ocean observations from drifter/floats show the role of horizontal density gradient in setting the stratification within the mixed layer. McWilliams et al. (2009) computed vertical turbulent mixing within the boundary layer in a one-dimensional vertical column using the K-profile parameterization (KPP) scheme with surface mean wind stress, mean heating, and solar absorption, and idealized representations of the heat flux from the interior three dimensional circulation and found that there is not a single, simple paradigm for the upper-ocean velocity profiles in stratified Ekman layers due to the following reasons: (a) the Ekman layer is compressed by stable stratification and surface heating; (b) Ekman currents penetrate down into the stratified layer; (c) penetrative solar absorption deepens the mean Ekman

layer; (d) wind and especially buoyancy rectification effects yield a mean Ekman profile with a varying eddy viscosity, where the mean turbulent stress and mean shear are not aligned, whereas buoyancy rectification induces profile flattening. These modeling results are for the one-dimensional ocean, i.e., no horizontal gradients of any variables including the density.

Effect of ocean surface gravity waves on the Ekman spiral has been identified through interacting waves with ocean currents and wind stresses. As waves experience breaking and dissipation, momentum passes from waves into ocean currents. Recent studies show that the influence of the surface wave motion via the Stokes drift and mixing is important to understanding the observed Ekman current profiles in addition to wind stress, depth-varying eddy viscosity, and density inhomogeneity. Song and Huang (2011) used the WKB method to obtain the analytic solutions for modified Ekman equations including random surface wave effects when the eddy viscosity is gradually varying with depth. Their solution was compared with observational data and with the results from a large eddy simulation of the Ekman layer (Zikanov et al. 2003).

However, effect of horizontally inhomogeneous density on the Ekman spiral with varying eddy viscosity due to vertical mixing under various surface forcing conditions has not yet been studied. Since horizontally inhomogeneous density leads to non-zero vertical geostrophic shear, and in turn contributes to the current shear, the equations and surface boundary conditions for the classical Ekman model need to be modified. Such modifications may lead to a new structure of the Ekman spiral. The baroclinic components of the Ekman spiral are identified analytically in this study using the KPP and three existing (due to pure wind forcing) eddy viscosities without considering ocean waves. Rest of the paper is organized as follows. Section 2 introduces the basic equations and boundary conditions. Sections 3 and 4 describe the Obukhov length scale

(Obukhov 1946, Monin and Obukhov 1954), depth ratio, and KPP. Section 5 presents the

analytical solution of the Ekman spiral in horizontally inhomogeneous ocean including analytical

barotropic and baroclinic components due to KPP eddy viscosity. Section 6 and 7 describe the

baroclinic effects with the KPP eddy viscosity under both surface wind and buoyancy forcing

and with the three existing eddy viscosities under pure wind forcing.   Section 8 presents the

conclusions. Appendices A and B list the procedures for obtaining the analytical solutions of the

Ekman spiral in horizontally inhomogeneous ocean with depth-dependent eddy viscosity.

2. Ekman Layer Dynamics

Let (x, y, z) be the zonal (positive eastward), latitudinal (positive northward), and vertical

(positive upward with $z = 0$ at the ocean surface) coordinates with $(\mathbf{i}, \mathbf{j}, \mathbf{k})$ as the corresponding

unit vectors, and $\hat{\mathbf{u}}$ be the velocity vector. Following the similar steady dynamics of McWilliams

and Huckle (2006) with modification from homogeneous to inhomogeneous density, the steady-

state horizontal momentum balance with Boussinesq approximation is given by

$$f\mathbf{k} \times \hat{\mathbf{u}} = -\frac{1}{\rho_w}\nabla p - \frac{1}{h}\frac{\partial}{\partial \sigma}(\mathbb{M}), \qquad (1a)$$

where $\rho_w = 1025$ kg m^{-3}, is the characteristic density of seawater; h is the ocean surface mixed

layer depth; $\sigma = -z/h$, is the non-dimensional vertical coordinate; f is the Coriolis parameter

(depending on the latitude); $\mathbb{M}$ is the vertical momentum flux due to turbulent mixing; p is the

pressure. It is noted that the damping for currents due to vertical radiation of inertial waves into

the oceanic interior is neglected. The mixed layer depth (h) can be determined from temperature

and density profiles using subjective and objective methods (e.g., Monterey and Levitus 1997;

Chu et al. 2002; Chu and Fan 2010, 2011). The hydrographic balance gives

$$\frac{1}{\rho_w}\frac{\partial p}{\partial z} = g - g\frac{\rho}{\rho_w}, \qquad (1b)$$

6

where ρ is the density; g is the gravitational acceleration (9.81 m s^{-2}).

The horizontal velocity consists of two parts: geostrophic current, $[\hat{\mathbf{u}}_g = (\hat{u}_g, \hat{v}_g)]$, and ageostrophic current $[\hat{\mathbf{u}}_E = (\hat{u}_E, \hat{v}_E)]$ (Ekman flow),

$$\hat{\mathbf{u}} = \hat{\mathbf{u}}_g + \hat{\mathbf{u}}_E. \tag{2}$$

where the geostrophic current is given by

$$f\mathbf{k} \times \hat{\mathbf{u}}_g = -\frac{1}{\rho_w} \nabla p, \tag{3}$$

and computed solely from the density field (Chu 1995; 2000; 2006). Differentiation of (3) with respect to z and use of (1b) lead to the thermal wind relation

$$\frac{\partial \hat{\mathbf{u}}_g}{\partial z} = -\mathbf{k} \times \left(\frac{g}{f \rho_w} \nabla \rho \right). \tag{4}$$

Substitution of (2)-(3) into (1a) leads to

$$f\mathbf{k} \times \hat{\mathbf{u}}_E = -\frac{1}{h} \frac{\partial}{\partial \sigma} (\mathbb{M}). \tag{5}$$

The vertical momentum flux $\mathbb{M}$ (i.e., turbulent Reynolds stress) is modeled by

$$\mathbb{M}(z) = -\frac{\hat{K}}{h} \frac{\partial \hat{\mathbf{u}}}{\partial \sigma}, \tag{6a}$$

where $\hat{K}$ is the eddy viscosity that is non-dimensionalized by

$$K = \frac{\hat{K}}{h \kappa u_*}, \tag{6b}$$

where $\kappa = 0.41$, is the von Karmen constant. Substitution of (2) into (6a) and use of (6b) lead to

$$\mathbb{M}(z) = -\kappa u_* K \left(\frac{\partial \hat{\mathbf{u}}_g}{\partial \sigma} + \frac{\partial \hat{\mathbf{u}}_E}{\partial \sigma} \right). \tag{7}$$

The velocity ($\hat{\mathbf{u}}_E$) is nondimesionalized by

$$\mathbf{u}_E = \frac{\hat{\mathbf{u}}_E}{V_E}, \quad V_E \equiv \frac{u_*^2}{\sqrt{2|f|\hat{K}(0)}}, \tag{8}$$

where $\hat{K}(0)$ is the eddy viscosity evaluated at the surface. Substitution of (7) into (5) and use of (4) and (8) give

$$f\mathbf{k}\times\mathbf{u}_E - \frac{\kappa u_*}{h}\frac{\partial}{\partial\sigma}\left[K\frac{\partial\mathbf{u}_E}{\partial\sigma}\right] = \frac{\kappa u_*}{fV_E}\mathbf{k}\times\frac{\partial}{\partial\sigma}[K\mathbf{S}], \quad \mathbf{S}\equiv\frac{g}{\rho_w}\nabla\rho \tag{9}$$

Here, the vector, $\mathbf{S} = (s_x, s_y)$, is defined by

$$s_x = \frac{g}{\rho_w}\frac{\partial\rho}{\partial x}, \quad s_y = \frac{g}{\rho_w}\frac{\partial\rho}{\partial y}, \tag{10}$$

which represents the baroclinicity (i.e., $s_x \neq 0, \ s_y \neq 0$). The ocean is barotropic if

$$s_x = s_y = 0. \tag{11}$$

The second-order differential equation (9) needs two boundary conditions. At the surface $(\sigma = 0)$ we have

$$\mathbb{M}(0) = \frac{\hat{\tau}}{\rho_w} = C_D\frac{\rho_a}{\rho_w}|\hat{\mathbf{u}}_a|\hat{\mathbf{u}}_a \equiv u_*^2\boldsymbol{\theta}_* \tag{12a}$$

where C_D is the drag coefficient; $\hat{\tau}$ is the surface wind stress; $\rho_a = 1.29$ kg m^{-3}, is the characteristic atmospheric density; $\hat{\mathbf{u}}_a$ is the wind near the ocean surface; $\boldsymbol{\theta}_* = [\cos\theta, \ \sin\theta]$ is the unit vector of the wind direction; θ is the angle of the wind from the east; and u_* is the ocean friction velocity,

$$u_* = \left[\frac{C_D\rho_a|\hat{\mathbf{u}}_a|^2}{\rho_w}\right]^{1/2}. \tag{12b}$$

Evaluation of (7) and (4) at the surface leads to

$$\mathbb{M}(0) = -\kappa u_* K\left(\frac{\partial\hat{\mathbf{u}}_g}{\partial\sigma} + \frac{\partial\hat{\mathbf{u}}_E}{\partial\sigma}\right)_{\sigma=0}, \tag{13a}$$

8

$$\left(\frac{\partial \hat{\mathbf{u}}_g}{\partial \sigma}\right)_{\sigma=0} = \mathbf{k} \times \left(\frac{gh}{f\rho_w}\nabla\rho\right)_{\sigma=0}. \qquad (13b)$$

Substitution of (10), (12a), and (13b) into (13a) leads to the surface boundary condition for the non-dimensional Ekman flow $\mathbf{u}_E$,

$$\left(\frac{\partial \mathbf{u}_E}{\partial \sigma}\right)_{\sigma=0} = -\frac{u_*}{\kappa K(0)V_E}\boldsymbol{\theta}_* - \frac{h}{fV_E}\mathbf{k}\times\mathbf{S}(0). \qquad (14)$$

where $K(0)$ and $\mathbf{S}(0)$ represent the values of $(K, \mathbf{S})$ evaluated at the surface ($\sigma = 0$). Moreover, the general solution of (9) contains exponentially increasing and decreasing parts with the non-dimensional depth σ. The exponentially increasing part is unphysical and needs to be eliminated. Therefore, the lower boundary condition of equation (9) is used

$$\mathbf{u}_E \text{ finite as } \sigma \to \infty \qquad (15)$$

to filter out the unphysical solution. In fact, the lower boundary condition (15) is also used in the classical Ekman spiral.

Generally, equation (9) is not closed. One more equation for the density ρ is needed. If ρ is given, the second-order differential equation (9) with the boundary conditions (14) and (15) are well-posed. For depth-dependent eddy viscosity, (9) is an inhomogeneous linear differential equation with variable coefficient K.

3. Obukhov Length (L) and Depth Ratio (λ)

The eddy viscosity is to characterize vertical mixing, which is generated by surface wind stress ($\boldsymbol{\tau}$) and surface buoyancy flux (B in $m^2\ s^{-3}$, upward positive),

$$B = \frac{g\alpha Q}{\rho(0)c_p} + g\beta(E-P)S, \qquad (16)$$

where Q is the net heat flux (upward positive, $W\ m^{-2}$); c_p is the specific heat for the sea water; S is the surface salinity [in practical salinity units (psu)]; α is the coefficient of thermal expansion;

9

β is the coefficient of haline contraction; and (E, P) are evaporation and precipitation (m s^{-1}).

Ocean mixed layer is generally developed by wind stirring and convection (upward surface buoyancy flux B). To examine dominant mixing mechanisms, the Obukhov length scale (L) and the depth ratio (λ) are calculated by

$$L = -\frac{u_*^3}{\kappa B}, \quad \lambda = \frac{h}{L} = \frac{(10 \text{ m})}{L} \frac{h}{(10 \text{ m})}. \qquad (17)$$

Here, L is the depth where the wind-generated turbulence is balanced by the downward buoyancy flux ($B < 0$) due to surface warming ($Q < 0$) and/or freshening ($P > E$) and is comparable to the convection-generated turbulence by the upward buoyancy flux ($B > 0$) due to surface cooling ($Q > 0$) and/or salinization ($P < E$); and λ is the depth ratio. Monthly depth ratio (λ) (Fig. 1) are calculated from the monthly mean global ocean (10 m)/L and ocean friction velocity (u_*) data ($1^{\circ} \times 1^{\circ}$) downloaded from http://iridl.ldeo.columbia.edu/SOURCES/.DASILVA/.SMD94/.climatology/ (DaSilva et al. 1994), and the monthly mixed layer depth (h) data downloaded from http://www.nodc.noaa.gov/OC5/WOA94/mix.html (Monterey and Levitus 1997).

The depth ratio (λ) is used to determine the forcing regimes (Lombardo and Gregg 1989): convective regime ($\lambda < -10$), wind-forcing regime ($\lambda > -1$), and combined forcing regime ($-10 \leq \lambda \leq -1$). The depth ratio (λ) also serves as a stability parameter (see next section). The calculated monthly depth ratio (λ) (Fig. 1) shows strong seasonal variability with only two regimes evident: wind-forcing and combined forcing regimes since almost no data with $\lambda < -10$. In January, the combined forcing ($-10 \leq \lambda \leq -1$) prevails most of the northern hemisphere including North Atlantic, North Pacific, Arabian Sea, Mediterranean Sea, and eastern tropical South Pacific; and the wind forcing ($\lambda > -1$) prevails most of the southern hemisphere. In July,

10

the combined forcing prevails in the southern hemisphere; and the wind forcing prevails in the northern hemisphere.

4. KPP

With the surface wind and buoyancy forcing, the KPP rules for the non-dimensional eddy viscosity (K) are given by the product of a depth-dependent non-dimensional turbulent velocity $w_x(\sigma)$ (scaled by κu_*) and a dimensionless vertical shape function $G(\sigma)$ (Large et al. 1994)

$$K(\sigma, \lambda) = \begin{cases} w_x(\sigma, \lambda)G(\sigma), & \text{if } 1 \geq \sigma \geq 0 \\ w_x(1, \lambda)G(1), & \text{if } \sigma > 1 \end{cases}, \qquad (18)$$

to represent the capability of deeper mixed layers to contain larger more effect turbulent eddies. It is noted that the extension of eddy viscosity $K(\sigma, \lambda)$ from $1 \geq \sigma \geq 0$ to $\sigma \geq 0$ is due to the fact that h was defined as the boundary layer depth in the original KPP model, which is usually deeper than the mixed layer depth. The shape function $G(\sigma)$ is assumed to be a cubic polynomial (O'Brien 1970) and given by (McWilliams and Huckle 2006) (Fig. 2)

$$G(\sigma) = \sigma\left[1 - \sigma^2\right] + \frac{(\sigma_0 - \sigma)^2}{2\sigma_0} H(\sigma_0 - \sigma), \qquad (19)$$

where $\sigma_0 = 0.05$, $H(a)$ is the Heaviside step function (equal to 1 for $a > 0$ and 0 otherwise). As pointed out by McWilliams and Huckle (2006), the second term in the righthand side of (19) is the mathematical aesthetics and computational regularity.

The depth dependent non-dimensional turbulent velocity scale $w_x(\sigma)$ is given by (Large et al. 1994)

$$w_x(\sigma, \lambda) = \begin{cases} \dfrac{1}{\phi(\varepsilon\lambda)}, & \varepsilon < \sigma < 1 \quad \lambda < 0, \quad \varepsilon = 0.1 \\ \dfrac{1}{\phi(\sigma\lambda)}, & \text{otherwise} \end{cases} \qquad (20)$$

11

Here, the function ϕ is defined by the Monin-Obukhov similarity theory (Monin and Obukhov 1954) such that the dimensional turbulent velocity scales equal κu_* with neutral forcing ($\lambda = 0$) and are enhanced and reduced in unstable ($\lambda < 0$) and stable ($\lambda > 0$) conditions. It is given by (Large et al. 1994)

$$\phi(\sigma\lambda) = \begin{cases} 1 + 5\sigma\lambda, & 0 \le \lambda \\ (1 - 16\sigma\lambda)^{-1/4}, & \lambda < 0, \ \sigma \le \alpha_m / \lambda \\ (1.26 - 8.38\sigma\lambda)^{-1/3}, & \lambda < 0, \ \sigma > \alpha_m / \lambda \end{cases} \qquad \alpha_m = -0.2 \qquad (21)$$

For neutral forcing ($\lambda = 0$), $\phi(\sigma\lambda) = 1$. Substitution of (19), (20), and (21) into (18) leads to an analytical non-dimensional KPP eddy viscosity $K(\sigma, \lambda)$. For a given depth σ, ϕ increases with λ (Fig. 3a); and $K(\sigma, \lambda)$ decreases with λ (Fig. 3b). Such λ-dependence of ϕ and $K(\sigma, \lambda)$ is quite smooth for $\lambda > 0$ and $\lambda < 0$, but very abrupt at $\lambda = 0$. The ϕ- values are small for $\lambda < 0$ (e.g., $\phi = 0.05$ for $\sigma = 0.5$, $\lambda = -1$) and very large for $\lambda > 0$ (e.g., $\phi \approx 30,000$ for $\sigma = 0.5$, $\lambda = 1$). The K-values are large for $\lambda < 0$ (e.g., $K \simeq 7$ for $\sigma = 0.5$, $\lambda = -1$) and very small for $\lambda > 0$ (e.g., $K \approx 10^{-5}$ for $\sigma = 0.5$, $\lambda = 1$). However, the dependence of ϕ and $K(\sigma, \lambda)$ on σ is quite mild. Substitution of the KPP eddy viscosity at the surface $K(0, \lambda)$ into (8) leads to

$$V_E = \frac{u_*^{3/2}}{\sqrt{2|f|h\kappa K(0,\lambda)}}$$

Monthly Ekman velocity scale (V_E), calculated from the same data sets for the computation of λ, has strong seasonal variability (Fig. 4). In January, larger V_E-values (> 0.5 m s^{-1}) occur in the northern hemisphere such as in the Gulf Stream, Kuroshio, equatorial regions (especially in the eastern Pacific), and smaller V_E-values (< 0.2 m s^{-1}) occur in the southern hemisphere. In July, smaller V_E-values (< 0.2 m s^{-1}) occur in the northern hemisphere except

some northern tropical regions such as near the northern African coast and west Arabian Sea, and

larger V_E-values (> 0.5 m s^{-1}) occur in the southern hemisphere.

5. Ekman Spiral

Substitution of (18) into (9) leads to

$$f\mathbf{k} \times \mathbf{u}_E - \frac{\kappa u_*}{h} \frac{\partial}{\partial \sigma}\left[K(\sigma,\lambda)\frac{\partial \mathbf{u}_E}{\partial \sigma}\right] = \frac{\kappa u_*}{fV_E}\mathbf{k} \times \frac{\partial}{\partial \sigma}\left[K(\sigma,\lambda)\mathbf{S}\right], \tag{22}$$

which is an ordinary differential equation with depth-varying $K(\sigma, \lambda)$.   The WKB method was

used in this study to solve the differential equation (22) with the boundary conditions (14) and

(15) to get the approximate analytical solutions $\mathbf{u}_E$ [$= (u_E, v_E)$] (see Appendix A),

$$u_E = \bar{u}_E + \Delta u_E, \quad v_E = \bar{v}_E + \Delta v_E, \tag{23}$$

where

$$\bar{u}_E = \exp\left[F(\sigma,\lambda)\right]\left\{\alpha^+ \cos\left[F(\sigma,\lambda)\right] + \alpha^- \sin\left[F(\sigma,\lambda)\right]\right\}, \tag{24a}$$

$$\bar{v}_E = \exp\left[F(\sigma,\lambda)\right]\left\{\alpha^+ \sin\left[F(\sigma,\lambda)\right] - \alpha^- \cos\left[F(\sigma,\lambda)\right]\right\} \tag{24b}$$

are the barotropic components of the Ekman velocity (i.e., $s_x = 0$, $s_y = 0$); and

$$\Delta u_E = \gamma \exp\left[F(\sigma,\lambda)\right]\left\{\beta^+ \cos\left[F(\sigma,\lambda)\right] + \beta^- \sin\left[F(\sigma,\lambda)\right]\right\}$$

$$-\frac{\gamma\,\mathrm{sgn}(f)}{2f^2}\int_0^\sigma \left[\begin{array}{l} \left\{\left[\dfrac{\partial\left[\sqrt{K(\zeta,\lambda)}(s_x - s_y)\right]}{\partial\zeta} + (s_x - s_y)\dfrac{\partial\sqrt{K(\zeta,\lambda)}}{\partial\zeta}\right]\cos\left[F(\sigma,\lambda) - F(\zeta,\lambda)\right]\right. \\[2em] \left. -\left[\dfrac{\partial\left[\sqrt{K(\zeta,\lambda)}(s_x + s_y)\right]}{\partial\zeta} + (s_x + s_y)\dfrac{\partial\sqrt{K(\zeta,\lambda)}}{\partial\zeta}\right]\sin\left[F(\sigma,\lambda) - F(\zeta,\lambda)\right]\right\} \\[2em] \times\exp\left(\left[F(\sigma,\lambda) - F(\zeta,\lambda)\right]\right) \end{array}\right]d\zeta$$

$$-\frac{\gamma\,\mathrm{sgn}(f)}{2f^2}\int_\sigma^\infty\left\{\left[\left[\frac{\partial\left[\sqrt{K(\zeta,\lambda)}(s_x-s_y)\right]}{\partial\zeta}+(s_x-s_y)\frac{\partial\sqrt{K(\zeta,\lambda)}}{\partial\zeta}\right]\cos\left[F(\sigma,\lambda)-F(\zeta,\lambda)\right]\right.\right.$$
$$\left.+\left[\frac{\partial\left[\sqrt{K(\zeta,\lambda)}(s_x+s_y)\right]}{\partial\zeta}+(s_x+s_y)\frac{\partial\sqrt{K(\zeta,\lambda)}}{\partial\zeta}\right]\sin\left[F(\sigma,\lambda)-F(\zeta,\lambda)\right]\right]$$
$$\left.\times\exp\left(-\left[F(\sigma,\lambda)-F(\zeta,\lambda)\right]\right)\right\}d\zeta$$

(25)

$$\Delta v_E=\gamma\exp\left[F(\sigma,\lambda)\right]\left\{\beta^+\sin\left[F(\sigma,\lambda)\right]-\beta^-\cos\left[F(\sigma,\lambda)\right]\right\}$$

$$-\frac{\gamma\,\mathrm{sgn}(f)}{2f^2}\int_0^\sigma\left\{\left[\left[\frac{\partial\left[\sqrt{K(\zeta,\lambda)}(s_x+s_y)\right]}{\partial\zeta}+(s_x+s_y)\frac{\partial\sqrt{K(\zeta,\lambda)}}{\partial\zeta}\right]\cos\left[F(\sigma,\lambda)-F(\zeta,\lambda)\right]\right.\right.$$
$$\left.+\left[\frac{\partial\left[\sqrt{K(\zeta,\lambda)}(s_x-s_y)\right]}{\partial\zeta}+(s_x-s_y)\frac{\partial\sqrt{K(\zeta,\lambda)}}{\partial\zeta}\right]\sin\left[F(\sigma,\lambda)-F(\zeta,\lambda)\right]\right]$$
$$\left.\times\exp\left(\left[F(\sigma,\lambda)-F(\zeta,\lambda)\right]\right)\right\}d\zeta$$

$$-\frac{\gamma\,\mathrm{sgn}(f)}{2f^2}\int_\sigma^\infty\left\{\left[\left[\frac{\partial\left[\sqrt{K(\zeta,\lambda)}(s_x+s_y)\right]}{\partial\zeta}+(s_x+s_y)\frac{\partial\sqrt{K(\zeta,\lambda)}}{\partial\zeta}\right]\cos\left[F(\sigma,\lambda)-F(\zeta,\lambda)\right]\right.\right.$$
$$\left.-\left[\frac{\partial\left[\sqrt{K(\zeta,\lambda)}(s_x-s_y)\right]}{\partial\zeta}+(s_x-s_y)\frac{\partial\sqrt{K(\zeta,\lambda)}}{\partial\zeta}\right]\sin\left[F(\sigma,\lambda)-F(\zeta,\lambda)\right]\right]$$
$$\left.\times\exp\left(-\left[F(\sigma,\lambda)-F(\zeta,\lambda)\right]\right)\right\}d\zeta$$

(26)

are the baroclinic components of the Ekman velocity (i.e., nonzero if $s_x\neq0$, $s_y\neq0$). The

parameters are defined as follows:

$$\gamma\equiv\frac{\kappa h|f|\sqrt{K(0,\lambda)}}{u_*},\quad \alpha^\pm\equiv(\cos\theta\pm\sin\theta)\,\mathrm{sgn}(f),\quad \mathrm{sgn}(f)=\begin{cases}1,&\text{if }f\geq0\\-1,&\text{if }f<0\end{cases}$$

(27)

14

$$\beta^+ \equiv -2\operatorname{sgn}(f)\sqrt{K(0,\lambda)}s_y(0)/f^2$$

$$+\frac{\operatorname{sgn}(f)}{f^2}\int_0^\infty \left\{ \begin{array}{l} \left[\dfrac{\partial\left[\sqrt{K(\sigma,\lambda)}s_y\right]}{\partial\sigma}+s_y\dfrac{\partial\sqrt{K(\sigma,\lambda)}}{\partial\sigma}\right]\cos\left[F(\sigma,\lambda)\right] \\[2em] +\left[\dfrac{\partial\left[\sqrt{K(\sigma,\lambda)}s_x\right]}{\partial\sigma}+s_x\dfrac{\partial\sqrt{K(\sigma,\lambda)}}{\partial\sigma}\right]\sin\left[F(\sigma,\lambda)\right] \end{array} \right\}\exp\left[F(\sigma,\lambda)\right]d\sigma \qquad (28a)$$

$$\beta^- \equiv 2\operatorname{sgn}(f)\sqrt{K(0,\lambda)}s_x(0)/f^2$$

$$+\frac{\operatorname{sgn}(f)}{f^2}\int_0^\infty \left\{ \begin{array}{l} \left[\dfrac{\partial\left[\sqrt{K(\sigma,\lambda)}s_y\right]}{\partial\sigma}+s_y\dfrac{\partial\sqrt{K(\sigma,\lambda)}}{\partial\sigma}\right]\sin\left[F(\sigma,\lambda)\right] \\[2em] -\left[\dfrac{\partial\left[\sqrt{K(\sigma,\lambda)}s_x\right]}{\partial\sigma}+s_x\dfrac{\partial\sqrt{K(\sigma,\lambda)}}{\partial\sigma}\right]\cos\left[F(\sigma,\lambda)\right] \end{array} \right\}\exp\left[F(\sigma,\lambda)\right]d\sigma \qquad (28b)$$

$$F(\sigma,\lambda)=-\sqrt{\frac{|f|h}{2\kappa u_*}}\int_0^\sigma \frac{d\varsigma}{\sqrt{K(\varsigma,\lambda)}} . \qquad (29)$$

Here, $\operatorname{sgn}(f)$ is the sign function.

The nondimensional barotropic $(\bar{u}_E,\bar{v}_E)$, and baroclinic $(\Delta u_E,\Delta v_E)$ components of the Ekman spiral are calculated for the global oceans except the regions near the equator (5^oS – 5^oN) using (24a), (24b), (25a), (25b) with the monthly mean global ocean density ρ (kg m^{-3}) calculated from the World Ocean Atlas 2009 temperature and salinity data ($1^o \times 1^o$ resolution) (http://www.nodc.noaa.gov/OC5/WOA09/pubwoa09.html) using the International Thermodynamic Equation of Seawater (http://www.teos-10.org/pubs/TEOS-10_Manual.pdf), the computed KPP eddy viscosity data $K(\sigma, \lambda)$, the ocean friction velocity (u_*) data ($1^o \times 1^o$) from http://iridl.ldeo.columbia.edu/SOURCES/.DASILVA/.SMD94/.climatology/ (DaSilva et al. 1994), the monthly mixed layer depth (h) data from http://www.nodc.noaa.gov/OC5/WOA94/mix.html (Monterey and Levitus 1997), and the angle

of surface wind (θ) data, which is computed from the monthly zonal wind data downloaded from

the website: http://iridl.ldeo.columbia.edu/SOURCES/.DASILVA/.SMD94/.climatology/.u3/ and

the monthly meridional wind data downloaded from the website:

http://iridl.ldeo.columbia.edu/SOURCES/.DASILVA/.SMD94/.climatology/.v3/.

Fig. 5 shows examples of dimensional Ekman spirals ($\hat{\mathbf{u}}_E = V_E \mathbf{u}_E$) with (solid curve)

and without (dashed curve) baroclinic components. The upper left panels (a), and (b) show the

Ekman spirals at Location-1 (11°N, 159°W) (i.e., north equatorial Pacific) with large baroclinic

components. The upper right panels (c), and (d) indicate the Ekman spirals at Location-2 (43°N,

169°E) (i.e., northwestern Pacific mid-latitude) with small baroclinic components. Profiles of the

horizontal density gradient ($\partial \rho / \partial x, \partial \rho / \partial y$) are much larger at Location-1 (lower left panels)

than at Location-2 (lower right panels).

6. Baroclinic Effect

The baroclinic portion of the Ekman spiral can be effectively determined by the ratio of

the vertical integration of baroclinic Ekman component over the Ekman velocity,

$$M = \frac{\int_0^\infty \sqrt{\Delta u_E^2 + \Delta v_E^2} \, d\sigma}{\int_0^\infty \sqrt{u_E^2 + v_E^2} \, d\sigma} . \tag{30}$$

Horizontal distribution of M has strong seasonal and spatial variability with large M-values ($>$

0.2) occurring in the tropical North Pacific Ocean, tropical Atlantic Ocean (10°N – 25°N), and

eastern Arabian Sea with the largest value of 0.9 in the central tropical North Pacific Ocean near

the dateline, and with small M-values (< 0.2) occurring in the southern hemisphere in January,

and vice versa in July (Fig. 6). Comparison between Fig. 6 and Fig. 1 shows negative correlation

between λ and M: large (small) λ corresponds to small (large) M. Such negative correlation is

16

found in the scatter diagrams of (λ, M) for the global oceans in January (Fig. 7a) and July (Fig. 7b) with linear regression equations,

$$M = 0.0239 - 0.0195\lambda \quad (R^2 = 0.561) \quad \text{for January}, \qquad (31)$$

$$M = 0.0305 - 0.0171\lambda \quad (R^2 = 0.463) \quad \text{for July}. \qquad (32)$$

The two regression equations are significant on the level of 0.0005 with the numbers of paired data are 6945 in January (Fug. 7a) and 6940 in July (Fig. 7b). The negative correlation between λ and M may be related to the increase of the KPP eddy viscosity with the decrease of λ especially for $\lambda < 0$.

The baroclinicity parameter is identified by the vertical integration of the magnitude of horizontal s – gradient (crossing the mixed layer) scaled by f^2,

$$b = \frac{1}{f^2} \int_0^\infty \sqrt{s_x^2 + s_y^2} \, d\sigma, \qquad (33)$$

which shows evident spatial variability and weak seasonal variability (Fig. 8). Since B is inversely proportional to f^2, the B-value is usually large ($B > 5$) in low latitudes (20°S – 20°N), and small ($B \leq 5$) in middle and high latitudes. It is noted that the scale factor of f^2 for the baroclinicity parameter (B) [see (33)] (scaled by f^2) is only used for searching for baroclinic Ekman components since ($\Delta u_E, \Delta v_E$) are inversely proportional to f^2 [see (25), (26), (28a), and (28b)].

The baroclinic effect on the Ekman spiral is evaluated by the correlation coefficient (R) between the two parameters, M and b, under the wind ($\lambda \geq -1$ and combined ($\lambda < -1$) forcing regimes in the northern and southern hemisphere (Table 1). It is found that M and b are positively correlated for all the situations with large R (> 0.73) for both hemispheres and months (January and July) under the surface wind forcing regime ($\lambda \geq -1$, with large R in the northern

hemisphere in January (0.77) and in the southern hemisphere in July (0.62) under the combined forcing regime ($\lambda < -1$), and with small R in the northern hemisphere in July (0.49) and in the southern hemisphere in January (0.36).

The scatter diagrams of (b, M) for the northern hemisphere (Fig. 9) and southern hemisphere (Fig. 10) also show the similar statistical relationships between M and b (M increase as B increases). Since M vanishes as b vanishes, (i.e., no baroclinic Ekman components when the horizontal density gradient equals zero), the linear regression equation between M and b is written by

$$M = cb, \tag{34}$$

where the regression coefficient c is obtained using the least square error method. The regression coefficient c is always positive (Table 1). It has largest value under the combined forcing regime in January for the northern hemisphere (0.0498), and in July for the southern hemisphere (0.0370). It has smallest value under the combined forcing regime in July for the northern hemisphere (0.00551) (prevailing wind forcing regime), and in January for the southern hemisphere (0.00932) (prevailing wind forcing regime). Thus, the baroclinic effect is enhanced in the hemisphere with prevailing combined forcing regime and weakened in the hemisphere with prevailing wind forcing regime.

7. Eddy Viscosity due to Pure Wind Forcing

7.1. General Description

Earlier studies such as in McWilliams and Huckle (2006) and Song and Huang (2011) assume no surface buoyancy flux (B = 0), i.e., the depth ratio λ = 0 [see (17)], the depth dependent non-dimensional turbulent velocity scale $w_x(\sigma)$ equals 1 [see (20) and (21)]. Also, the dimensional form of the Ekman equation is used

$$f\mathbf{k} \times \hat{\mathbf{u}}_E - \frac{\partial}{\partial z}\left[\hat{K}(z)\frac{\partial \hat{\mathbf{u}}_E}{\partial z}\right] = -\frac{1}{f}\mathbf{k} \times \frac{\partial}{\partial z}\left[\hat{K}(z)\mathbf{S}\right], \tag{35}$$

with the surface (dimensional) boundary condition,

$$\hat{K}(0)\left(\frac{\partial \hat{\mathbf{u}}_E}{\partial z}\right)_{z=0} = u_*^2\hat{\boldsymbol{\theta}}_* + \mathbf{k} \times \left(\frac{\hat{K}(0)\mathbf{S}(0)}{f}\right), \tag{36a}$$

and the lower boundary condition,

$$\hat{\mathbf{u}}_E \text{ finite as } z \to -\infty, \tag{36b}$$

where

$$\hat{K}(0) = 0.004u_*^2 / |f|. \tag{36c}$$

With the monthly mean surface wind stress data, the ocean friction velocity u_* [using (12b)] and

in turn the surface eddy viscosity $\hat{K}(0)$ [using (36c)] are calculated except the equatorial region

5°S – 5°N. Fig. 11 clearly shows strong horizontal and seasonal variations of $\hat{K}(0)$. In January, it

has large values (> 0.02 m^2 s^{-1}) in the western/central tropical North Pacific and Atlantic oceans

(6°N – 25°N), medium values (0.01 – 0.02 m^2 s^{-1}) in the mid-latitudes associated with the

Kuroshio and Gulf Stream, and small values (< 0.01 m^2 s^{-1}) in rest of the global oceans.

However, in July, it has very large values (> 0.03 m^2 s^{-1}) in the western Arabian Sea (related to

the Southwest monsoon), large values (0.02 – 0.03 m^2 s^{-1}) in the western Bay of Bengal and the

southern tropical Indian and Atlantic oceans (6°S – 25°S), medium values (0.01 – 0.02 m^2 s^{-1}) in

the southern tropical Pacific Ocean (6°S – 25°S), mid-latitude (35°S - 45°S) Indian Ocean, and

small values (< 0.01 m^2 s^{-1}) in rest of global oceans in July.

The eddy viscosity $\hat{K}(z)$ has three different types: (a) wind and depth dependent using

the KPP, (b) wind dependent and depth independent, i.e., taking surface value $\hat{K}(0)$ for the

whole water column, and (c) wind and depth independent, i.e., assigning a constant value. Correspondingly, the solutions for the three types of eddy viscosity are represented by $\hat{\mathbf{u}}_E^{(1)}$, $\hat{\mathbf{u}}_E^{(2)}$, $\hat{\mathbf{u}}_E^{(3)}$,

$$\hat{u}_E^{(i)} = \hat{\bar{u}}_E^{(i)} + \Delta \hat{u}_E^{(i)}, \quad \hat{v}_E^{(i)} = \hat{\bar{v}}_E^{(i)} + \Delta \hat{v}_E^{(i)}, \quad i = 1, 2, 3 \tag{37}$$

where $(\hat{\bar{u}}_E^{(i)}, \hat{\bar{v}}_E^{(i)})$ are the components of the Ekman velocity in barotropic ocean [i.e., the Ekman solutions when (11) is satisfied]; and $(\Delta \hat{u}_E^{(i)}, \Delta \hat{v}_E^{(i)})$ are the baroclinic components of the Ekman spiral. The baroclinic effect is identified by the root-mean square (RMS) within the ocean mixed layer of the baroclinic components $[(\Delta \hat{u}_E^{(1)}, \Delta \hat{v}_E^{(1)}), (\Delta \hat{u}_E^{(2)}, \Delta \hat{v}_E^{(2)}), (\Delta \hat{u}_E^{(3)}, \Delta \hat{v}_E^{(3)})]$,

$$R_i = \sqrt{\frac{1}{J} \sum_{j=1}^{J} \left\{ \left[\Delta \hat{u}_E^{(i)}(j) \right]^2 + \left[\Delta \hat{v}_E^{(i)}(j) \right]^2 \right\}}, \quad i = 1, 2, 3 \tag{38}$$

where j denotes the vertical level; and J is the total number of the vertical levels from the surface to the mixed layer depth.

7.2. Wind and Depth Dependent Eddy Viscosity

The vertically varying eddy viscosity due to the surface wind stress is given by (Song and Huang 2011)

$$\hat{K}(z) = \hat{K}(0)(1 - \alpha_1 z) \exp(\alpha_2 z), \tag{39}$$

where (α_1, α_2) are positive constants. Fitting (37) with the flow in the *f*-plane using the large-eddy simulations (Zikanov et al. 2003) gives the following semi-empirical formula (Song and Huang 2011)

$$\hat{K}(z) = \hat{K}(0)\bar{G}(\frac{|f|z}{u_*}), \quad \bar{G}(t) = (1 - 64.0327t) \exp(4.0073t), \tag{40}$$

to calculate the depth-dependent eddy viscosity due to the surface wind stress. Here, $\bar{G}(t)$ is the shape function. Fig. 12 shows the dependence of $\bar{G}(t)$ versus t, where t is the non-dimensional depth, $t = |f| z / u_*$. It is noted that $\hat{K}(0)$ is inversely proportional to the magnitude of the Coriolis parameter $|f|$. For the same ocean friction velocity u_*, the lower the latitude, the higher the value of $\hat{K}(0)$.

The Ekman velocity, $\hat{\mathbf{u}}_E^{(1)} = [\hat{u}_E^{(1)}, \hat{v}_E^{(1)}]$ are the approximate analytical solutions of (35) by the WKB method (see Appendices A and B) with the eddy viscosity $\hat{K}(z)$ given by (40). The barotropic components are given by

$$\hat{u}_E^{(1)} = \exp[F(z)]\left\{\hat{V}^+ \cos[F(z)] + \hat{V}^- \sin[F(z)]\right\}, \tag{41a}$$

$$\hat{v}_E^{(1)} = \exp[F(z)]\left\{\hat{V}^+ \sin[F(z)] - \hat{V}^- \cos[F(z)]\right\}, \tag{41b}$$

where

$$\hat{V}^\pm = V_E \alpha^\pm \, \mathrm{sgn}(f), \qquad F(z) = -\sqrt{\frac{|f|}{2}} \int_z^0 \frac{d\zeta}{\sqrt{\hat{K}(\zeta)}} \tag{42}$$

The baroclinic components are given by

$$\Delta \hat{u}_E^{(1)} = \exp[F(z)]\left\{\Delta_1 \hat{V}^+ \cos[F(z)] + \Delta_1 \hat{V}^- \sin[F(z)]\right\}$$

$$+ \frac{[s_x(0) - s_y(0)]}{4f} \int_z^0 \sqrt{\frac{2}{|f|\hat{K}(\zeta)}} \left\{\frac{\partial \hat{K}(\zeta)}{\partial \zeta} \cos[F(z) - F(\zeta)]\right\} \exp\left([F(z) - F(\zeta)]\right) d\zeta$$

$$- \frac{[s_x(0) + s_y(0)]}{4f} \int_z^0 \sqrt{\frac{2}{|f|\hat{K}(\zeta)}} \left\{\frac{\partial \hat{K}(\zeta)}{\partial \zeta} \sin[F(z) - F(\zeta)]\right\} \exp\left([F(z) - F(\zeta)]\right) d\zeta \tag{43a}$$

$$+ \frac{[s_x(0) - s_y(0)]}{4f} \int_{-\infty}^z \sqrt{\frac{2}{|f|\hat{K}(\zeta)}} \left\{\frac{\partial \hat{K}(\zeta)}{\partial \zeta} \cos[F(z) - F(\zeta)]\right\} \exp\left(-[F(z) - F(\zeta)]\right) d\zeta$$

$$+ \frac{[s_x(0) + s_y(0)]}{4f} \int_{-\infty}^z \sqrt{\frac{2}{|f|\hat{K}(\zeta)}} \left\{\frac{\partial \hat{K}(\zeta)}{\partial \zeta} \sin[F(z) - F(\zeta)]\right\} \exp\left(-[F(z) - F(\zeta)]\right) d\zeta$$

21

$$\Delta \hat{v}_E^{(1)} = \exp\left[F(z)\right]\left\{\Delta_1 \hat{V}^+ \sin\left[F(z)\right] - \Delta_1 \hat{V}^- \cos\left[F(z)\right]\right\}$$

$$+ \frac{[s_x(0) - s_y(0)]}{4f} \int_z^0 \sqrt{\frac{2}{|f|\hat{K}(\zeta)}} \left\{\frac{\partial \hat{K}(\zeta)}{\partial \zeta} \sin\left[F(z) - F(\zeta)\right]\right\} \exp\left(\left[F(z) - F(\zeta)\right]\right) d\zeta$$

$$+ \frac{[s_x(0) + s_y(0)]}{4f} \int_z^0 \sqrt{\frac{2}{|f|\hat{K}(\zeta)}} \left\{\frac{\partial \hat{K}(\zeta)}{\partial \zeta} \cos\left[F(z) - F(\zeta)\right]\right\} \exp\left(\left[F(z) - F(\zeta)\right]\right) d\zeta \qquad (43b)$$

$$+ \frac{[s_x(0) + s_y(0)]}{4f} \int_{-\infty}^z \sqrt{\frac{2}{|f|\hat{K}(\zeta)}} \left\{\frac{\partial \hat{K}(\zeta)}{\partial \zeta} \cos\left[F(z) - F(\zeta)\right]\right\} \exp\left(-\left[F(z) - F(\zeta)\right]\right) d\zeta$$

$$- \frac{[s_x(0) - s_y(0)]}{4f} \int_{-\infty}^z \sqrt{\frac{2}{|f|\hat{K}(\zeta)}} \left\{\frac{\partial \hat{K}(\zeta)}{\partial \zeta} \sin\left[F(z) - F(\zeta)\right]\right\} \exp\left(-\left[F(z) - F(\zeta)\right]\right) d\zeta$$

Here

$$\Delta_1 \hat{V}^+ = -\sqrt{\frac{\hat{K}(0)}{2|f|}} \frac{s_y(0)}{f} - \frac{s_y(0)}{2\sqrt{2}f\sqrt{|f|}} \int_{-\infty}^0 \frac{\exp\left[F(z)\right]}{\sqrt{\hat{K}(z)}} \left\{\frac{\partial \hat{K}(z)}{\partial z} \cos\left[F(z)\right]\right\} dz$$

$$- \frac{s_x(0)}{2\sqrt{2}f\sqrt{|f|}} \int_{-\infty}^0 \frac{\exp\left[F(z)\right]}{\sqrt{\hat{K}(z)}} \left\{\frac{\partial \hat{K}(z)}{\partial z} \sin\left[F(z)\right]\right\} dz, \qquad (44a)$$

$$\Delta_1 \hat{V}^- = \sqrt{\frac{\hat{K}(0)}{2|f|}} \frac{s_x(0)}{f} + \frac{s_x(0)}{2\sqrt{2}f\sqrt{|f|}} \int_{-\infty}^0 \frac{\exp\left[F(z)\right]}{\sqrt{\hat{K}(z)}} \left\{\frac{\partial \hat{K}(z)}{\partial z} \cos\left[F(z)\right]\right\} dz$$

$$- \frac{s_y(0)}{2\sqrt{2}f\sqrt{|f|}} \int_{-\infty}^0 \frac{\exp\left[F(z)\right]}{\sqrt{\hat{K}(z)}} \left\{\frac{\partial \hat{K}(z)}{\partial z} \sin\left[F(z)\right]\right\} dz. \qquad (44b)$$

Fig. 13 shows the global horizontal distribution and zonal mean R_1 (m s^{-1}) in January and July. In January, it has large values (> 0.2 m s^{-1}) in the tropical North Pacific and Atlantic oceans (6$^{\rm o}$N – 20$^{\rm o}$N), the tropical North Indian Ocean (6$^{\rm o}$N – 10$^{\rm o}$N), the tropical South Pacific and Atlantic oceans (6$^{\rm o}$S – 10$^{\rm o}$S), medium values (0.02 – 0.2 m s^{-1}) in the mid-latitudes associated with the Kuroshio and Gulf Stream, south tropical Indian Ocean (6$^{\rm o}$S -30$^{\rm o}$S) and small values (< 0.01 m s^{-1}) in rest of the global oceans. In July, it has large values (> 0.2 m s^{-1}) in the tropical oceans (15$^{\rm o}$S – 15$^{\rm o}$N) with a maximum value of 0.62 m s^{-1} in the Arabian Sea. It generally decreases with the increasing latitude. In high latitudes, it is very small (< 0.01 m s^{-1}).

Zonal mean R_1 decreases with latitude near-exponentially in both northern and southern hemispheres) from 0.6 m s^{-1} (0.4 m s^{-1}) at 6°N (6°S) to less than 10^{-3} m s^{-1} at high latitudes near 60°N (60°S). The histograms and associated probability density functions (PDFs) for January and July (Fig. 14) show near-exponentially decreasing probability with R_1 (log scale used in the vertical axis). The probability of R_1 larger than 0.2 m s^{-1} is 2.6% [$=1 - P(R \leq 0.2 \text{ m s}^{-1}) = 1 - 0.974$)] in January and 4.6% ($= 1 - 0.954$) in July. The probability of R_1 larger than 0.1 m s^{-1} is 10.0% in January and 11.5% in July. The 95th percentile is 0.173 m s^{-1} in January and 0.212 m s^{-1} in July (also see Tables 2 and 3).

7.3. Wind-dependent and Depth-independent Eddy Viscosity

The eddy viscosity is given by

$$\hat{K}(z) = \hat{K}(0). \tag{45}$$

Substation of (45) into (42) leads to,

$$F(z) = \frac{z}{D_W}, \quad D_W = \sqrt{\frac{2\hat{K}(0)}{|f|}} = \sqrt{\frac{0.008 u_*^2}{|f|^{3/2}}}, \tag{46}$$

where (40) is used; D_w is the e-folding decay scale of the Ekman depth, which varies with the surface wind stress through $\hat{K}(0)$, and latitude. For the same ocean friction velocity (u_*), the lower the latitude, the higher the value of D_W. The e-folding scale D_w is computed from the global data of $\hat{K}(0)$ using (46). It also has evident horizontal and weak seasonal variations (Fig. 15, equatorial region 5°S – 5°N not computed): large values (> 100 m) generally occur in sub-tropical regions (10°N – 20°N, 10°S – 20°S) in January and July due to small Coriolis parameter. In the Northern Hemisphere middle and high latitudes, D_w is larger in January (50-100 m in the Atlantic Ocean and western Pacific Ocean) than in July (mostly less than 20 m).   In the Southern Hemisphere middle latitudes, zonal belts with medium values of D_w (20-50 m) appear

at 35°S $-$ 50°S in the three southern oceans (Atlantic, Indian, and Pacific) in January but does not appear in the Southern Pacific in July.

Substation of (46) into (41a), (41b), (43a), (43b), (44a) and (44b) leads to the barotropic components

$$\hat{\bar{u}}_E^{(2)} = \exp(\frac{z}{D_W})\left[\hat{V}^+\cos(\frac{z}{D_W}) + \hat{V}^-\sin(\frac{z}{D_W})\right], \tag{47a}$$

$$\hat{\bar{v}}_E^{(2)} = \exp(\frac{z}{D_W})\left[\hat{V}^+\sin(\frac{z}{D_W}) - \hat{V}^-\cos(\frac{z}{D_W})\right], \tag{47b}$$

and the baroclinic components

$$\Delta\hat{u}_E^{(2)} = \exp(\frac{z}{D_W})\left[\Delta_2\hat{V}^+\cos(\frac{z}{D_W}) + \Delta_2\hat{V}^-\sin(\frac{z}{D_W})\right], \tag{48a}$$

$$\Delta\hat{v}_E^{(2)} = \exp(\frac{z}{D_W})\left[\Delta_2\hat{V}^+\sin(\frac{z}{D_W}) - \Delta_2\hat{V}^-\cos(\frac{z}{D_W})\right]. \tag{48b}$$

Here $(\hat{V}^+, \hat{V}^-)$ are given by (42) and

$$\Delta_2\hat{V}^+ = -\frac{D_W s_y(0)}{f}, \quad \Delta_2\hat{V}^- = \frac{D_W s_x(0)}{2f}. \tag{49}$$

The global horizontal distribution of R_2 (m s^{-1}) (Fig. 16) is similar to that of R_1 (Fig. 13) in both January and July with smaller values in the Gulf Stream and Kuroshio regions. Latitudinal decrease of zonal mean RMS with the eddy viscosity is also comparable in both Northern and Southern Hemispheres. The histograms and associated PDFs for January and July (Fig. 17) also show near-exponentially decreasing probability with R_2. For large R_2 values (> 0.2 m s^{-1}), the probability is zero in January and 0.6% ($= 1 - 0.994$) in July. The probability of R_2 larger than 0.1 m s^{-1} is 0.28% in January and 4.7% in July. The 95th percentile is 0.089 m s^{-1} in January and 0.11 m s^{-1} in July.

7.4. Wind and Depth Independent Eddy Viscosity

For the wind and depth independent eddy viscosity,

$$\hat{K}(z) = \hat{K}_0 = \text{const}. \tag{50}$$

Substitution of (50) into (46) gives

$$D_W = D = \sqrt{\frac{2\hat{K}_0}{|f|}}, \tag{51}$$

which is the classical Ekman depth. After replacing D_W by D, (47a) and (47b) lead to the barotropic components $(\hat{\bar{u}}_E^{(3)}, \hat{\bar{v}}_E^{(3)})$ and (48a) and (48b) lead to the baroclinic components $(\Delta\hat{u}_E^{(3)}, \Delta\hat{v}_E^{(3)})$ of the Ekman velocity. Here, the constant eddy viscosity $\hat{K}_0$ is taken as 0.054 $\text{m}^2\ \text{s}^{-1}$ (Price et al. 1987).

The global horizontal distribution of R_3 (m s^{-1}) (Fig. 18) is similar to that of R_1 (Fig. 13) in January and July with latitudinal decrease of zonal mean RMS in the Northern and Southern Hemispheres. The histograms and associated PDFs for January and July (Fig. 19) also show near-exponentially decreasing probability with R_3. For large R_3 values (> 0.2 m s^{-1}), the probability is zero in January and July. The probability of R_3 larger than 0.1 m s^{-1} is 0.1% in January and 1.2% in July. The 95th percentile is 0.04 m s^{-1} in January and 0.058 m s^{-1} in July.

8. Conclusions

Analytical solution of the Ekman spiral in real oceans is obtained with vertical geostrophic and ageostrophic shears linking to turbulent stress in upper oceans, under surface wind and buoyancy forcing using the KPP eddy viscosity. The Ekman spiral contains barotropic and baroclinic components. The barotropic component is similar to the classical Ekman spiral. The baroclinic component is caused by horizontally inhomogeneous density. The baroclinic component vanishes as the horizontal density gradient vanishes.

25

Climatological monthly data of global ocean mixed layer depth, Monin-Obukhov length scale, friction velocity, surface winds, and density profiles are used to calculate the depth ratio (λ), KPP eddy viscosity, the barotropic and baroclinic Ekman velocities, the baroclinicity parameter (B), and the proportion of the baroclinic Ekman component (M). Large baroclinic proportion is usually associated with the prevailing combined forcing regime such as in the northern (southern) hemisphere in January (July).

Statistical analysis on the calculated global (λ, M, B) values shows significant negative correlation between λ and M: large (small) λ corresponds to small (large) M, and significant positive correlation between B and M: large (small) B corresponds to large (small) M. The negative correlation between λ and M may be related to the increase of the KPP eddy viscosity with the decrease of λ especially for $\lambda < 0$. The positive correlation coefficient between B and M varies with the prevailing wind and combined forcing regimes. The baroclinic effect is enhanced in the hemisphere with prevailing combined forcing regime and weakened in the hemisphere with prevailing wind forcing regime.

For pure wind forcing (i.e., zero surface buoyancy flux), three types of eddy viscosity from existing parameterization [wind and depth dependent, wind-dependent and depth-independent, and wind and depth independent (i.e., constant eddy viscosity)] as well as the vertical root-mean square of the baroclinic component within the ocean mixed layer (R) of the analytical Ekman spiral are used to investigate the baroclinic effect. It enhances with the decreasing latitude and usually very evident (> 0.2 m s^{-1}) in the tropical oceans in January and July, and extremely large value of 0.62 m s^{-1} in the Arabian Sea in July for all the cases (three types of eddy viscosity). In middle and high latitudes (especially in the South Hemisphere), it is generally very small (i.e., the classical Ekman spiral applies) except in the Gulf Stream and

Kuroshio regions in January. These results are consistent with the earlier observational studies such as conducted in the Drake Passage (Lenn and Chereskin 2009).

The near-exponentially decreasing probability with the vertical root-mean square of the baroclinic component is obtained from the histograms. The statistical characteristics show that the baroclinic components for the three types of eddy viscosity under pure wind forcing are all comparable in January and July. Near-exponentially decreasing probability with R_1, R_2, or R_3 is found. The probability of R_1 larger than 0.2 m s^{-1} is 2.6% [$=1 - P(R \leq 0.2$ m s$^{-1}) = 1 - 0.974)$] in January and 4.6% (= 1 − 0.954) in July. The probability of R_1 larger than 0.1 m s^{-1} is 10.0% in January and 11.5% in July. The 95th percentile is 0.173 m s^{-1} in January and 0.212 m s^{-1} in July (also see Tables 2 and 3).

Finally, it is noted that the monthly mean density fields from the WOA-2009 temperature and salinity data cannot represent density fronts associated with submesoscale processes. The computation here is only to show the importance of horizontally inhomogeneous density on the Ekman spiral. Further computation is needed to verify the good approximate/analytical solutions again high horizontal-resolution wind and density data if they will be available.

Appendix-A General Solutions of Eq(22)

Let the Ekman currents (u_E, v_E) be represented by a complex variable ψ,

$$\psi = u_E + iv_E, \quad i = \sqrt{-1}. \tag{A1}$$

Substitution of (A1) into (22) leads to

$$K\frac{d^2\psi}{d\sigma^2} + \frac{dK}{d\sigma}\frac{d\psi}{d\sigma} - if_0\psi = \phi, \tag{A2}$$

where

$$f_0 = \frac{fh}{\kappa u_*}, \quad \phi = \frac{h^2}{f_0 \kappa u_* V_E}\frac{\partial}{\partial\sigma}\left[Ks_y\right] - i\frac{h^2}{f_0 \kappa u_* V_E}\frac{\partial}{\partial\sigma}\left[Ks_x\right]. \tag{A3}$$

The function ϕ represents the baroclinic effect.

The second-order differential equation (A2) needs two boundary conditions. The surface boundary condition (14) becomes

$$\frac{d\psi}{d\sigma}\Big|_{\sigma=0} = -\frac{u_*}{\kappa K(0)V_E}\left(\cos\theta + i\sin\theta\right) + \frac{h^2}{f_0\kappa u_* V_E}[s_y(0) - is_x(0)]. \qquad (A4)$$

The lower boundary condition of equation (A2) is given by

$$|\psi| \quad \text{finite as} \quad \sigma \to \infty. \qquad (A5)$$

to guarantee a physically meaningful solution, i.e., $|\psi|$ cannot be infinity as $\sigma \to \infty$.

Eq. (A2) is a linear inhomogeneous ordinary differential equation with the depth-varying coefficient $K(z)$. Following Berger and Grisogono (1998), studying the Ekman atmospheric boundary layer, an approximate solution to the inhomogeneous problem (A2) can be found with the variation of parameters technique, provided that an approximate solution of the homogeneous problem of (A2),

$$K\frac{d^2\psi}{d\sigma^2} + \frac{dK}{d\sigma}\frac{d\psi}{d\sigma} - if_0\psi = 0, \qquad (A6)$$

exists. If two independent approximate solutions to homogeneous problem of Eq. (A6) are given by $\psi_1(\sigma)$ and $\psi_2(\sigma)$, the general solution of Eq. (A2) is given by

$$\psi = c_1\psi_1(\sigma) + c_2\psi_2(\sigma) + \hat{c}_1(\sigma)\psi_1(\sigma) + \hat{c}_2(\sigma)\psi_2(\sigma), \qquad (A7)$$

where

$$\hat{c}_1(\sigma) = -\int_\sigma^0 \frac{\psi_2\phi}{K(\zeta)[\psi_1(\zeta)d\psi_2(\zeta)/d\zeta - \psi_2(\zeta)d\psi_1(\zeta)/d\zeta]}d\zeta, \qquad (A8)$$

$$\hat{c}_2(\sigma) = \int_\sigma^\infty \frac{\psi_1\phi}{K(\zeta)[\psi_1(\zeta)d\psi_2(\zeta)/d\zeta - \psi_2(\zeta)d\psi_1(\zeta)/d\zeta]}d\zeta. \qquad (A9)$$

Appendix-B The WKB Method for Solving Eq.(A6)

The WKB method can be used to obtain a good approximate solution of Eq. (A6) if the vertical variation of $K(\sigma)$ is slower than that of $\psi(\sigma)$ (Grisogono 1995),

$$\psi \propto \exp\left[\frac{(S_0 + S_1\varepsilon + S_2\varepsilon^2 + ...)}{\varepsilon}\right], \tag{B1}$$

where ε is a presumably small parameter. Substitution of (B1) into (A6) leads to a set of equations in terms of powers of ε. If $K(\sigma)$ does not vary too quickly with depth, we have

$$\frac{|S_{n+1}(\sigma)|}{|S_n(\sigma)|} \ll 1, \quad n = 0,\ 1,\ 2,... \tag{B2}$$

Solving for the first two terms S_0 and S_1 yields

$$S_0 = \pm(1+i)\sqrt{\frac{|f_0|}{2}}\int_0^\sigma \frac{d\zeta}{\sqrt{K(\zeta)}}, \tag{B3}$$

$$S_1 = \frac{1}{4}\ln\left[\frac{K(0)}{K(\sigma)}\right]. \tag{B4}$$

Thus, the two approximate solutions of the homogeneous equation (A4) are

$$\psi_1(\sigma) = A(\sigma)\exp[(1+i)F(\sigma)], \quad \psi_2(\sigma) = A(\sigma)\exp[-(1+i)F(\sigma)], \tag{B5}$$

where

$$A(\sigma) = \left[\frac{K(0)}{K(\sigma)}\right]^{1/4}, \quad F(\sigma) = -\sqrt{\frac{|f_0|}{2}}\int_0^\sigma \frac{d\zeta}{\sqrt{K(\zeta)}}. \tag{B6}$$

Substitution of (B5) and (B6) into (A8) and (A9) gives

$$\hat{c}_1(\sigma) = -\frac{(1-i)}{2\sqrt{2|f_0|K(0)}}\int_0^\sigma A(\zeta)\phi(\zeta)\exp\left[-(1+i)F(\zeta)\right]d\zeta, \tag{B7}$$

$$\hat{c}_2(\sigma) = -\frac{(1-i)}{2\sqrt{2|f_0|K(0)}}\int_\sigma^\infty A(\zeta)\phi(\zeta)\exp\left[(1+i)F(\zeta)\right]d\zeta. \tag{B8}$$

Substitution of (B5) into (A7) gives

$$\psi = [c_1 + \hat{c}_1(\sigma)]A(\sigma)\exp[(1+i)F(\sigma)] + [c_2 + \hat{c}_2(\sigma)]A(\sigma)\exp[-(1+i)F(\sigma)]. \qquad \text{(B9)}$$

It is noted that $F(\sigma) < 0$ leads to

$$\psi_2 \to \infty \ \text{ as } \ \sigma \to \infty. \qquad \text{(B10)}$$

This leads to

$$c_2 = 0 \qquad \text{(B11)}$$

Substitution of (B9) into the surface boundary condition (A4) gives

$$c_1 = \hat{c}_2(0) + (1-i)\left\{\frac{u_*(\cos\theta + i\sin\theta)}{\kappa\sqrt{2|f_0|K(0)}} - \sqrt{\frac{K(0)}{|2f_0|}}\frac{h}{f}[s_y(0) - is_x(0)]\right\}.$$

$$= \hat{c}_2(0) + V^+ - iV^- + \sqrt{\frac{K(0)}{|2f_0|}}\frac{h}{f}\left\{\left[s_x(0) - s_y(0)\right] + i\left[s_x(0) + s_y(0)\right]\right\}.$$

$$\text{(B11)}$$

References

Chereskin, T.K. (1995). *Direct evidence for an Ekman balance in the California Current*. J. Geophys. Res., *100*, 18261–18269.

Chu, P.C. (1993). *Generation of low frequency unstable modes in a coupled equatorial troposphere and ocean mixed layer*. J. Atmos. Sci., *50*, 731-749.

Chu, P.C. (1995). *P-vector method for determining absolute velocity from hydrographic data*. Marine Tech. Soc. J., *29*, 2, 3-14.

Chu, P.C. (2000). *P-vector spirals and determination of absolute velocities*. J. Oceanogr., *56*, 591-599.

Chu, P. C. (2006). *P-Vector Inverse Method*. Springer, 605pp.

Chu, P.C., Garwood, R.W. Jr. (1991). *On the two-phase thermodynamics of the coupled cloud-ocean mixed layer*. J. Geophys. Res., *96*, 3425-3436.

Chu, P.C., Liu, Q.-Y., Jia, Y.-L., Fan, C.W. (2002). *Evidence of a barrier layer in the Sulu and Celebes Seas*. J. Phys. Oceanogr., *32*, 3299-3309.

Chu, P.C., Fan, C.W. (2010). *Optimal linear fitting for objective determination of ocean mixed layer depth from glider profiles*. J. Atmos. Oceanic Technol.*, 27*, 1893-1898.

Chu, P.C. & and Fan, C.W. (2011). *Maximum angle method for determining mixed layer depth from seaglider data*. J. Oceanogr., *67*, 219-230.

DaSilva, A., Young, A. C., Levitus, S. (1994). *Atlas of Surface Marine Data*, Volume 1: Algorithms and Procedures, Number 6, NOAA/NODC.

Ekman, V. W. (1905). *On the influence of the earth's rotation on ocean-currents*. Ark. Mat. Astron. Fys., *2*, 1–52.

Garwood, R.W. Jr. (1977). *An oceanic mixed layer capable of simulating cyclic states*. J. Phys. Oceanogr., *7*, 455-468.

Grachev A.A., Andreas E.L, Fairall C.W., Guest P.S., Persson P.O.G. (2008). *Turbulent measurements in the stable atmospheric boundary layer during SHEBA: ten years after*. Acta Geophysica. *56*, 1, 142-166.

Grisogono, B. (1995). *A generalized Ekman layer profile with gradually varying eddy diffusivities*. Quart. J. Roy. Meteorol. Soc. *121*, 445–453.

Hunkins, K. (1966). *Ekman drift currents in the Arctic Ocean*. Deep-Sea Res. *13*, 607–620.

Kraus, E. B., Turner, J.S. (1967). *A one-dimensional model of the seasonal thermocline, Part II*, Tellus, *19*, 98-105.

Large, W.G., McWilliams, J. C., Doney, S. C. (1994). *Oceanic vertical mixing: A review and a model with a non-local K-profile boundary layer parameterization*. Rev. Geophys.*, 32*, 363–403.

Lenn, Y., Chereskin, T.K. (2009). *Observation of Ekman Currents in the Southern Ocean*. J. Phys. Oceanogr., *39*, 768–779.

Lettau, H. H., Dabberdt, W. F. (1970). *Variangular Wind Spirals*. Boundary-Layer Meteorol. *1*, 64-79.

Lombardo, C. P., M. C. Gregg (1989). *Similarity scaling of viscous and thermal dissipation in a convecting surface boundary layer*, J. Geophys. Res., *94*, 6273–6284.

McWilliams, J. C., Huckle, E. (2006). *Ekman layer rectification*. J. Phys. Oceanogr., *36*, 1646-1659.

McWilliams, J. C., Huckle, E. & Shchepetkin, A. F. (2009). Buoyancy effects in a stratified Ekman layer. *J. Phys. Oceanogr.*, **39**, 2581–2599.

31

Monin, A. S., Obukhov, A. M. (1954). *Basic laws of turbulent mixing in the surface layer of the atmosphere*. Trudy Geofiz. Inst. Acad. Nauk SSSR., *24*, 163-187.

Monterey, G., Levitus, S. (1997). *Seasonal Variability of Mixed Layer Depth for the World Ocean*. NOAA Atlas NESDIS 14, U.S. Gov. Printing Office, Wash., D.C., 96 pp.

O'Brien, J. J. (1970). *A note on the vertical structure of the eddy exchange coefficient in the planetary boundary layer*. J. Atmos. Sci., *27*, 1213-1215.

Obukhov, A.M. (1946). *Turbulence in an atmosphere with a non‑uniform temperature*. Trudy Inst. Teoret. Geophys. Akad. Nauk SSSR. *1*: 95-115 (translation in: *Boundary‑Layer Meteorol*. 1971. 2: 7-29).

Price, J. F., Weller, R. A., Schudlich, R. R. (1987). *Wind-driven ocean currents and Ekman transport*. Science, *238*: 1534–1538.

Price, J. F., Sundermeyer, M.A. (1999). *Stratified Ekman layers*. J. Geophys. Res., *104*, 20467-20494.

Richman, J.F., deSzoeke, R., Davis, R.E. (1987). *Measurements of near-surface shear in the Ocean*. J. Geophys. Res., *92*, 2851–2858.

Song, J.-B., Huang, Y.-S. (2011). *An approximate solution of wave-modified Ekman current for gradually varying eddy viscosity*. Deep-Sea Res. I, *58*, 668–676.

Stacey, M.W., Pond, S., LeBlond, P. H. (1986). *A wind-forced Ekman spiral as a good statistical fit to low-frequency currents in a coastal strait*. Science, *233*, 470-472.

Steger, J., Collins, C.A., and Chu, P.C. (1998). *Circulation in the Archipelago de Colon (Galapagos Islands), November 1993*. Deep-Sea Res. II, *45*, 1093-1114.

Taylor, J. R., Sarkar, S. (2008). *Stratification effect in a bottom Ekman layer*. J. Phys. Oceanogr., *38*, 2535-2553.

Zikanov, O., Slinn, D.N., Dhanak, M.R. (2003). *Large-eddy simulations of the wind-induced turbulent Ekman layer*. J. Fluid Mech., *495*, 343–368.

Table 1. January and July correlation coefficients and number of paired data between (M, B) for northern and southern hemispheres under wind and combined forcing regimes.

Location	Statistics	January ($\lambda \geq -1$)	January ($\lambda < -1$)	July ($\lambda \geq -1$)	July ($\lambda < -1$)
Northern Hemisphere	Number of Paired Data	1181	1225	2120	143
	R	0.753	0.773	0.797	0.487
	c	0.00939	0.0498	0.0101	0.00551
Southern Hemisphere	Number of Paired Data	4015	220	2573	1660
	R	0.794	0.358	0.733	0.624
	c	0.0142	0.00932	0.0134	0.037

Table 2. Statistical characteristics of the VRMA (within the ocean mixed layer) of the baroclinic components over the global oceans for the three types of eddy viscosity under zero surface buoyancy flux in January.

RMS	$Q_{0.5}$ (m/s)	$Q_{0.95}$ (m/s)	$P(R \leq 0.02$ m/s)	$P(R \leq 0.1$ m/s)	$P(R \leq 0.2$ m/s)
R_1	0.0113	0.173	0.669	0.900	0.974
R_2	0.00401	0.0888	0.800	0.972	1.000
R_3	0.00107	0.0399	0.901	0.999	1.000

Table 3. Statistical characteristics of the VRMA (within the ocean mixed layer) of the baroclinic components over the global oceans for the three types of eddy viscosity under zero surface buoyancy flux in July.

RMS	$Q_{0.5}$ (m/s)	$Q_{0.95}$ (m/s)	$P(R \leq 0.02$ m/s)	$P(R \leq 0.1$ m/s)	$P(R \leq 0.2$ m/s)
R_1	0.00929	0.212	0.694	0.875	0.954
R_2	0.00306	0.110	0.795	0.953	0.994
R_3	0.000769	0.0575	0.883	0.988	1.000

Figure Captions

Fig. 1. Monthly depth ratio (λ): (a) January, and (b) July. It is noted that only two regimes are evident with the monthly mean data: wind-forcing and combined forcing regimes. Here, the black contours are referred as $\lambda = -1$.

Fig. 2. The shape function $G(\sigma)$.

Fig. 3. Dependence of (a) ϕ and (b) K on σ and λ for $1 \geq \sigma \geq 0$.

Fig. 4. Monthly Ekman velocity scale (V_E): (a) January, and (b) July.

Fig. 5. Examples of Ekman spirals (a) $\hat{u}_E$, (b) $\hat{v}_E$ at Location-1 (11°N, 159°W), (c) $\hat{u}_E$, and (d) $\hat{v}_E$ at Location-2 (43°N, 169°E) (upper panels) as well as corresponding horizontal density gradients (lower panels). It is noted that the horizontal density gradients are much stronger at Location-1 than Location-2.

Fig. 6. Monthly horizontal distribution of M: (a) January, and (b) July.
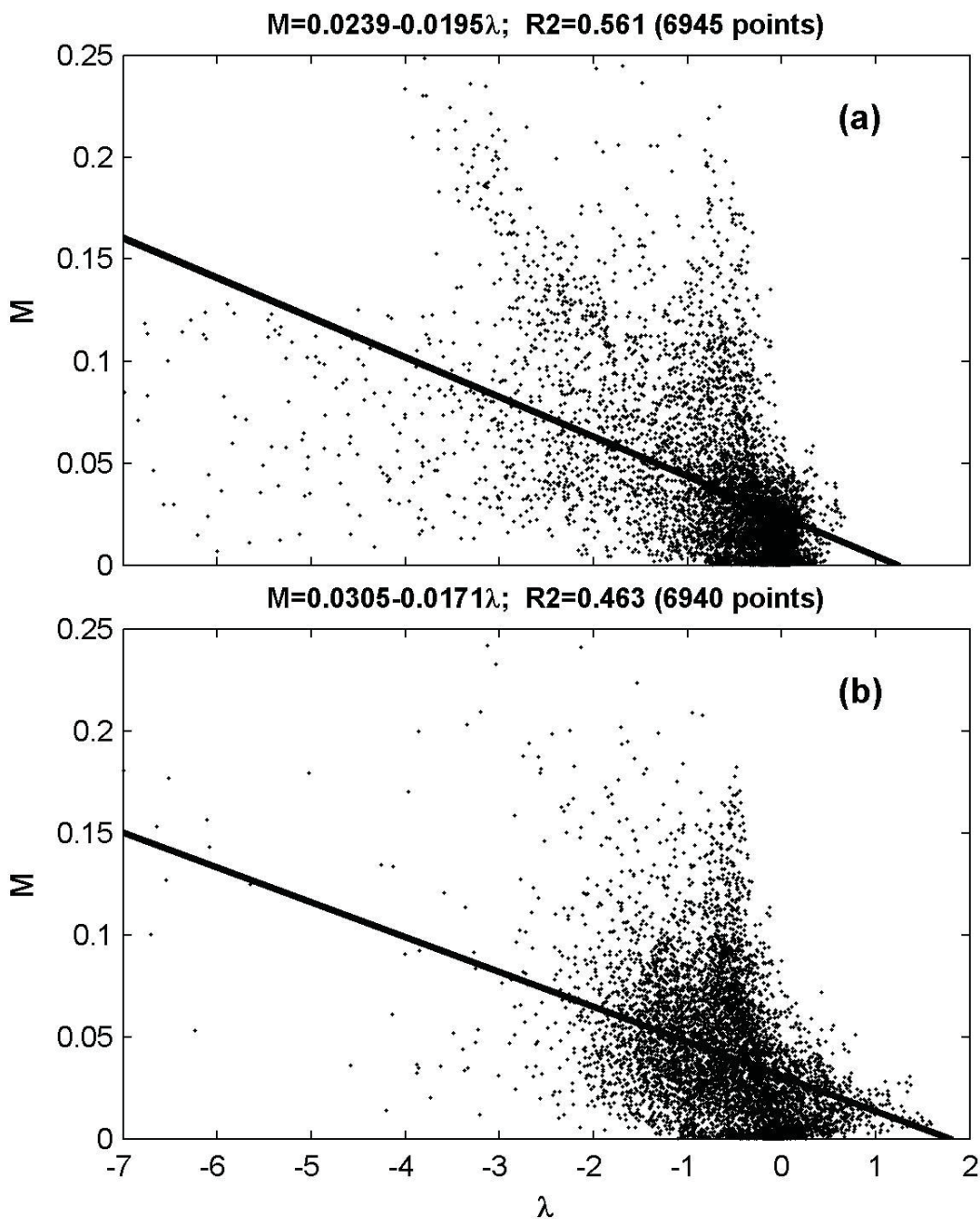
Fig. 7. Scatter diagrams of (λ, M) with linear regression: (a) January, and (b) July. It is noted that the negative correlation between (λ, M) is significant on the level of 0.0005.
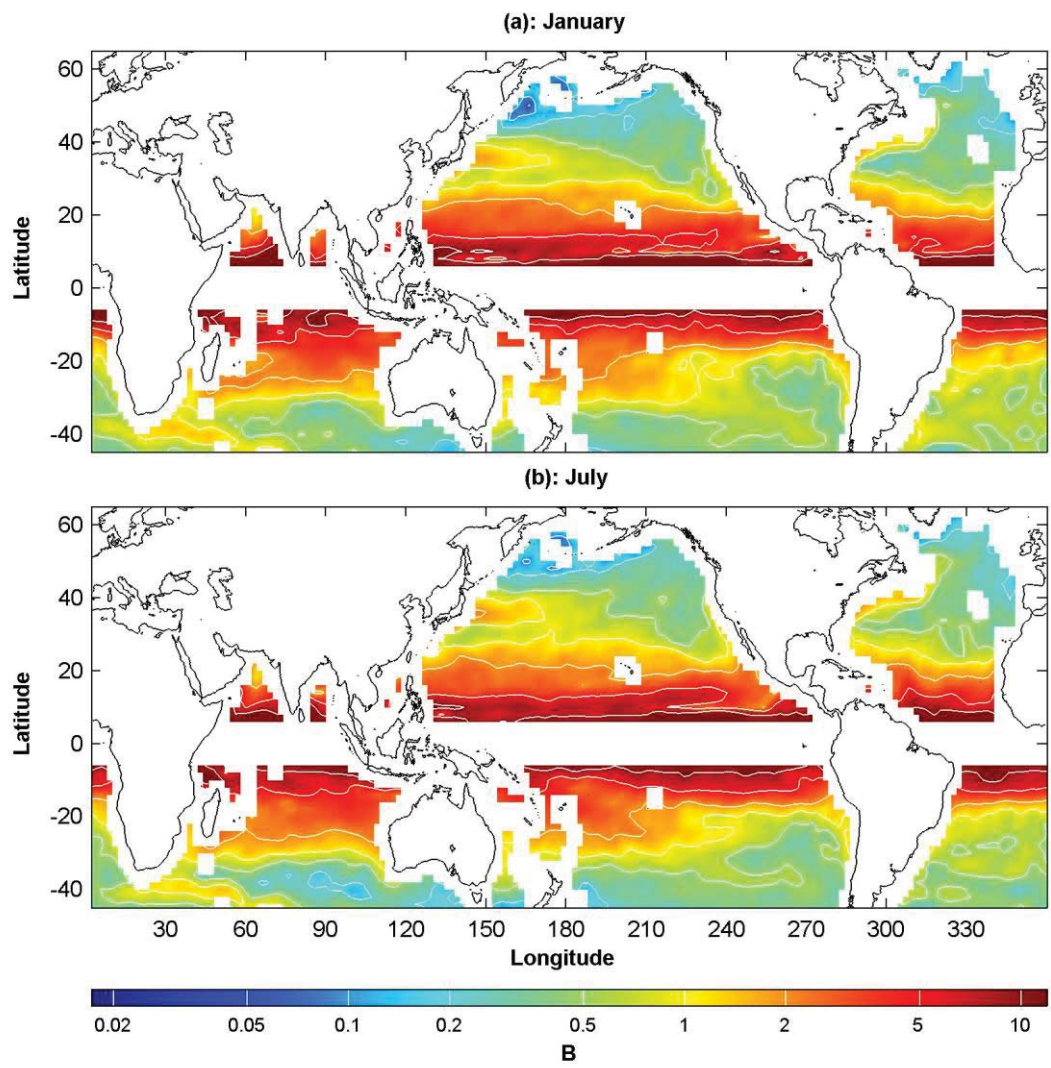
Fig. 8. Monthly horizontal distribution and zonal mean of B: (a) January, and (b) July.

Fig. 9. Scatter diagrams of (B, M) with linear regression for the northern hemisphere: (a) January, wind forcing regime ($\lambda \geq -1$, (b) January, combined forcing regime ($\lambda < -1$), (c) July, wind forcing regime ($\lambda \geq -1$, and (d) July, combined forcing regime ($\lambda < -1$). It is noted that the positive correlation between (λ, M) is significant on the level of 0.0005.
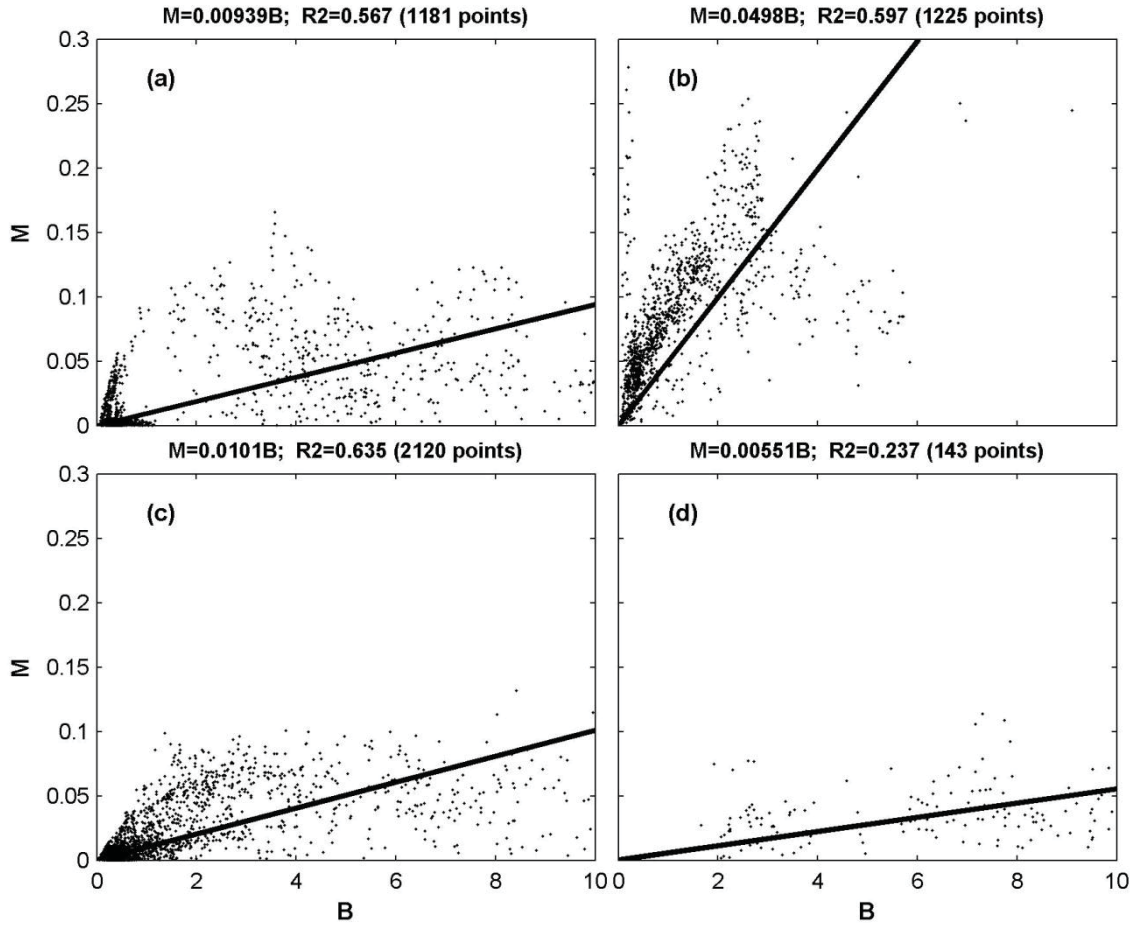
Fig. 10. Scatter diagrams of (B, M) with linear regression for the southern hemisphere: (a) January, wind forcing regime ($\lambda \geq -1$, (b) January, combined forcing regime ($\lambda < -1$), (c) July, wind forcing regime ($\lambda \geq -1$, and (d) July, combined forcing regime ($\lambda < -1$). It is noted that the positive correlation between (λ, M) is significant on the level of 0.0005.
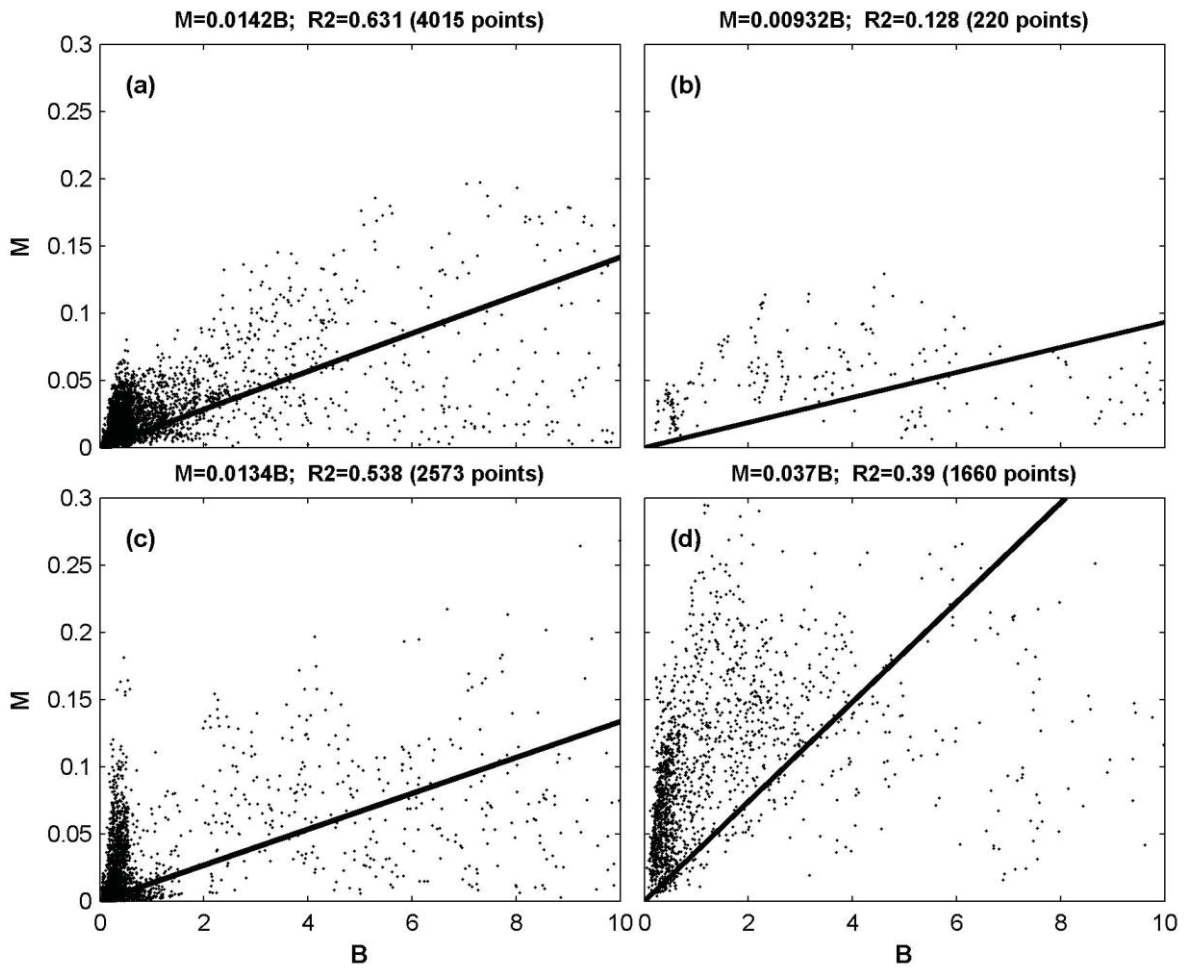
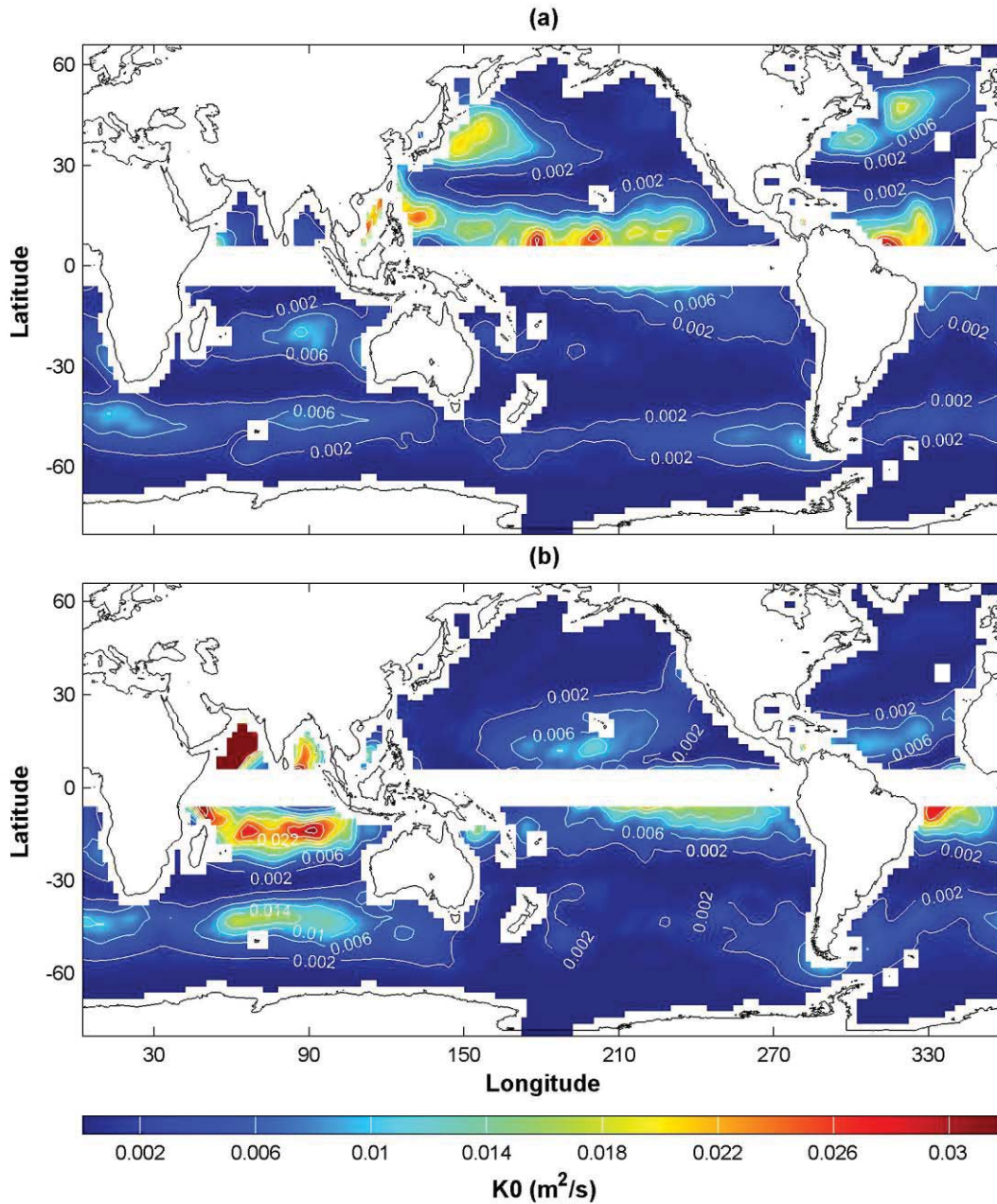Fig. 11. Horizontal distribution of eddy viscosity at the ocean surface $\hat{K}(0)$ calculated from monthly mean surface wind stress data (downloaded from the websites: http://iridl.ldeo.columbia.edu/SOURCES/.DASILVA/.SMD94/.climatology/.u3/ and http://iridl.ldeo.columbia.edu/SOURCES/.DASILVA/.SMD94/.climatology/.v3/ using (20) and (21): (a) January, and (b) July.

Fig. 12. Vertical structure function $\bar{G}(t)$ versus t.

Fig. 13.   Horizontal distribution and zonal mean of vertical root-mean square of baroclinic components of the Ekman spiral in neutral ocean, R_1 (m s^{-1}), inside the mixed layer with wind-dependent and depth-dependent eddy viscosity $K(z)$: (a), January, and (b) July.

Fig. 14. Histogram and probability density function of R_1 (m s^{-1}) with wind-dependent and depth-dependent eddy viscosity $\hat{K}(z)$: (a) January, and (b) July.

Fig. 15. Horizontal distribution of e-folding depth (D_w) of the Ekman layer with wind-dependent and depth-independent eddy viscosity: (a) January, and (b) July.

Fig. 16.   Horizontal distribution and zonal mean of vertical root-mean square of baroclinic components of the Ekman spiral in neutral ocean, R_2 (m s^{-1}), inside the mixed layer with wind-dependent and depth-independent eddy viscosity $\hat{K}(0)$: (a), January, and (b) July.

Fig. 17. Histogram and probability density function of R_2 (m s^{-1}) inside the mixed layer with wind-dependent and depth-independent eddy viscosity $\hat{K}(0)$: (a), January, and (b) July.

Fig. 18.   Horizontal distribution and zonal mean of vertical root-mean square of baroclinic components of the Ekman spiral in neutral ocean, R_3 (m s^{-1}), inside the mixed layer with a constant eddy viscosity (0.054 m^2 s^{-1}): (a), January, and (b) July.

Fig. 19. Histogram and probability density function of R_3 (m s^{-1}) inside the mixed layer with a constant eddy viscosity (0.054 m^2 s^{-1}): (a), January, and (b) July.

Fig. 1. Monthly depth ratio (λ): (a) January, and (b) July. It is noted that only two regimes are evident with the monthly mean data: wind-forcing and combined forcing regimes. Here, the black contours are referred as $\lambda = -1$.

Fig. 2. The shape function $G(\sigma)$.

Fig. 3. Dependence of (a) ϕ and (b) K on σ and λ for $1 \geq \sigma \geq 0$.

Fig. 4. Monthly Ekman velocity scale (V_E): (a) January, and (b) July.

Fig. 5. Examples of Ekman spirals (a) $\hat{u}_E$, (b) $\hat{v}_E$ at Location-1 (11°N, 159°W), (c) $\hat{u}_E$, and (d) $\hat{v}_E$ at Location-2 (43°N, 169°E) (upper panels) as well as corresponding horizontal density gradients (lower panels). It is noted that the horizontal density gradients are much stronger at Location-1 than Location-2.

40

Fig. 6. Monthly horizontal distribution of *M*: (a) January, and (b) July.

Fig. 7. Scatter diagrams of (λ, M) with linear regression: (a) January, and (b) July. It is noted that the negative correlation between (λ, M) is significant on the level of 0.0005.

Fig. 8. Monthly horizontal distribution and zonal mean of *B*: (a) January, and (b) July.

Fig. 9. Scatter diagrams of (B, M) with linear regression for the northern hemisphere: (a) January, wind forcing regime ($\lambda \geq -1$, (b) January, combined forcing regime ($\lambda < -1$), (c) July, wind forcing regime ($\lambda \geq -1$, and (d) July, combined forcing regime ($\lambda < -1$). It is noted that the positive correlation between (λ, M) is significant on the level of 0.0005.

Fig. 10. Scatter diagrams of (*B*, *M*) with linear regression for the southern hemisphere: (a) January, wind forcing regime ($\lambda \geq -1$, (b) January, combined forcing regime ($\lambda < -1$), (c) July, wind forcing regime ($\lambda \geq -1$, and (d) July, combined forcing regime ($\lambda < -1$). It is noted that the positive correlation between (λ, *M*) is significant on the level of 0.0005.

Fig. 11. Horizontal distribution of eddy viscosity at the ocean surface $\hat{K}(0)$ calculated from monthly mean surface wind stress data (downloaded from the websites: http://iridl.ldeo.columbia.edu/SOURCES/.DASILVA/.SMD94/.climatology/.u3/ and http://iridl.ldeo.columbia.edu/SOURCES/.DASILVA/.SMD94/.climatology/.v3/ using (20) and (21): (a) January, and (b) July.

Fig. 12. Vertical structure function $\bar{G}(t)$ versus t.

Fig. 13. Horizontal distribution and zonal mean of vertical root-mean square of baroclinic components of the Ekman spiral in neutral ocean, R_1 (m s^{-1}), inside the mixed layer with wind-dependent and depth-dependent eddy viscosity $K(z)$: (a), January, and (b) July.
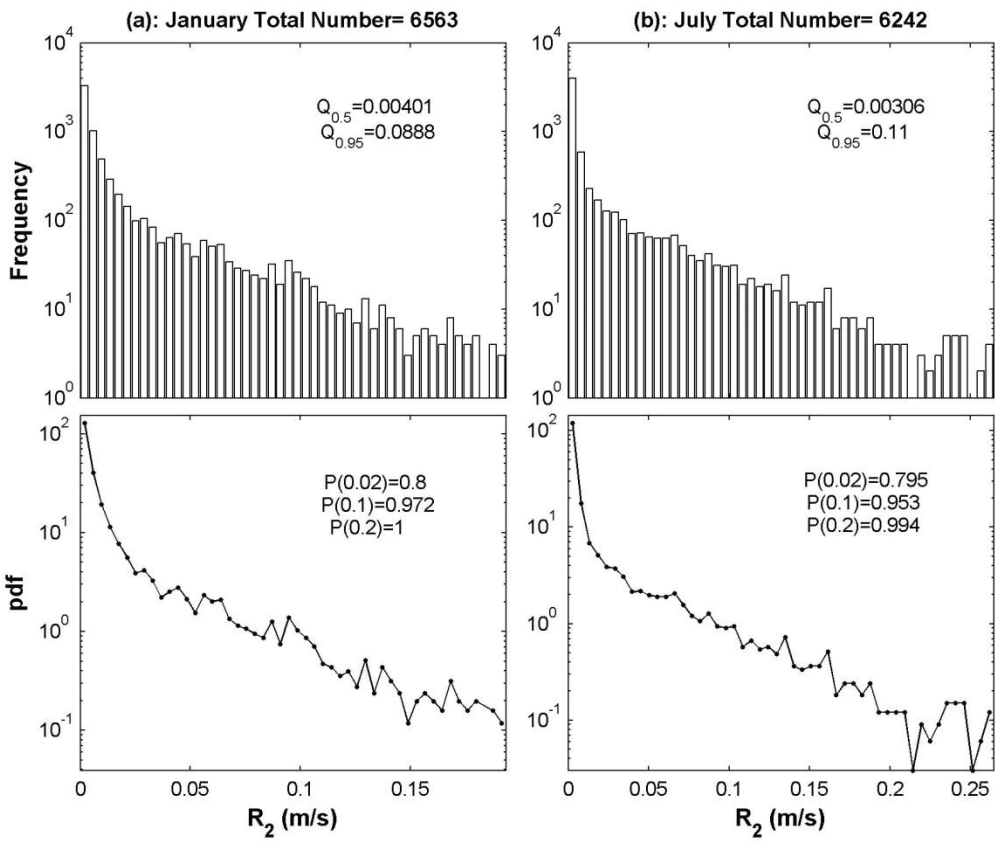
Fig. 14. Histogram and probability density function of R_1 (m s^{-1}) with wind-dependent and depth-dependent eddy viscosity $\hat{K}(z)$: (a) January, and (b) July.

Fig. 15. Horizontal distribution of e-folding depth (D_w) (unit: m) of the Ekman layer with wind-dependent and depth-independent eddy viscosity: (a) January, and (b) July.
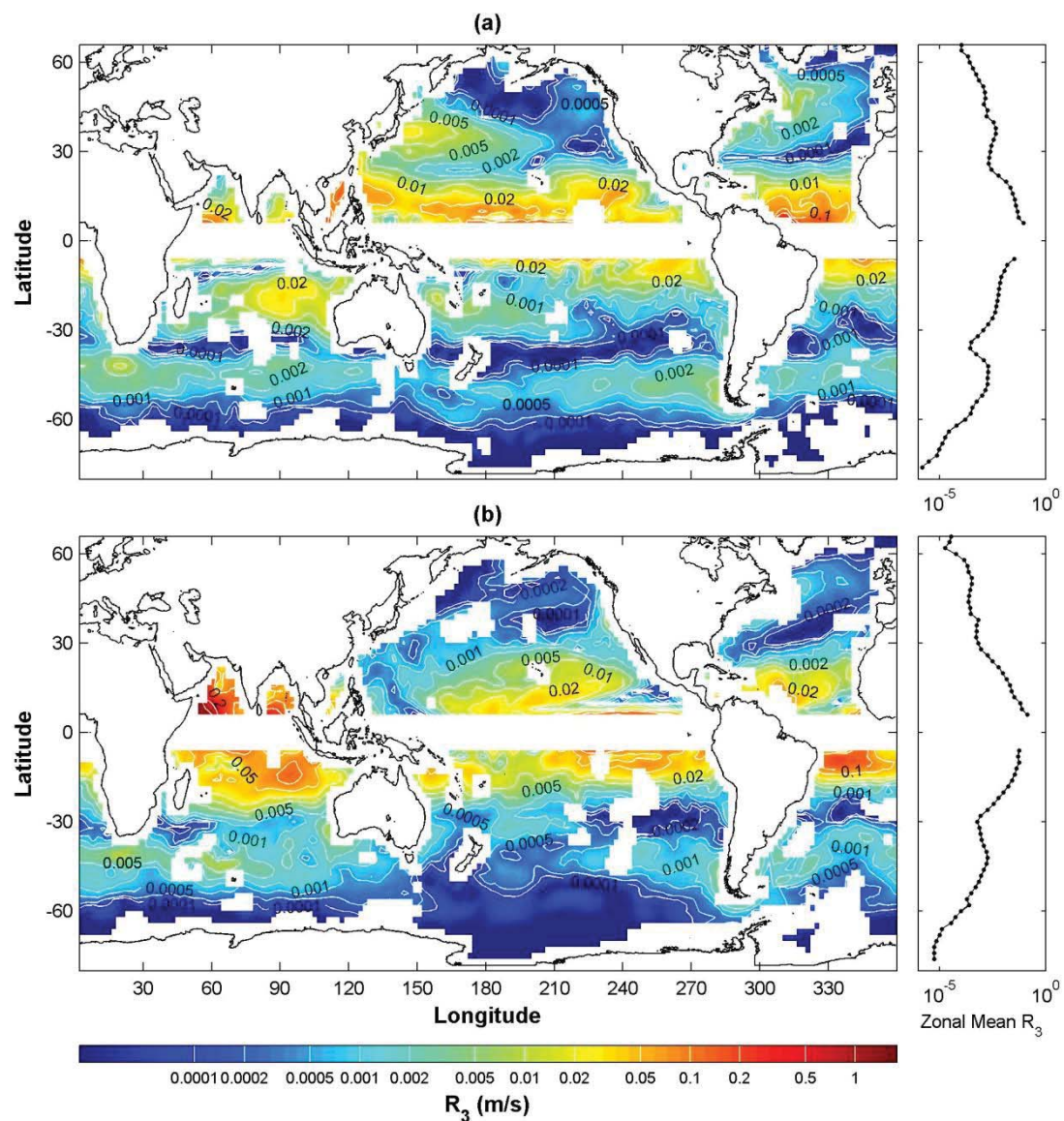
Fig. 16.   Horizontal distribution and zonal mean of vertical root-mean square of baroclinic components of the Ekman spiral in neutral ocean, R_2 (m s^{-1}), inside the mixed layer with wind-dependent and depth-independent eddy viscosity $\hat{K}(0)$: (a), January, and (b) July.

Fig. 17. Histogram and probability density function of R_2 (m s^{-1}) inside the mixed layer with wind-dependent and depth-independent eddy viscosity $\hat{K}(0)$: (a), January, and (b) July.

Fig. 18. Horizontal distribution and zonal mean of vertical root-mean square of baroclinic components of the Ekman spiral in neutral ocean, R_3 (m s^{-1}), inside the mixed layer with a constant eddy viscosity (0.054 m^2 s^{-1}): (a), January, and (b) July.
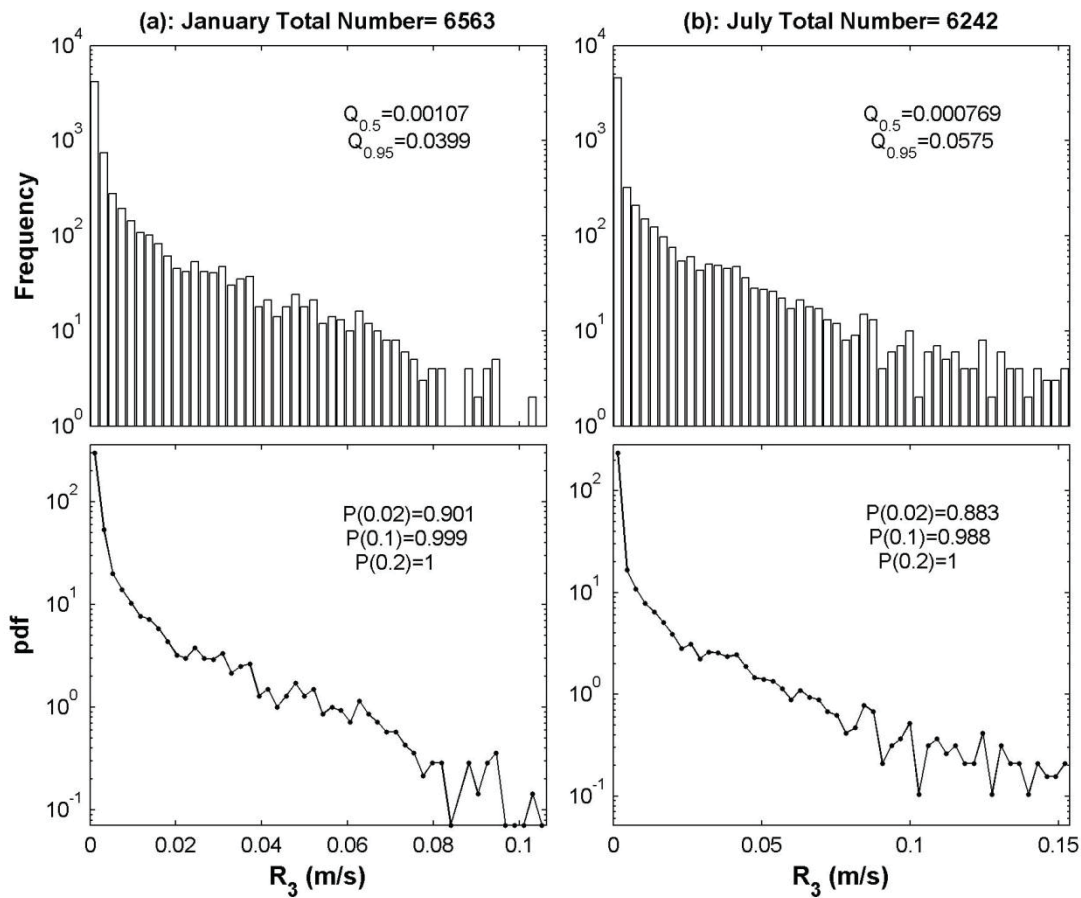
Fig. 19. Histogram and probability density function of R_3 (m s^{-1}) inside the mixed layer with a constant eddy viscosity (0.054 m^2 s^{-1}): (a), January, and (b) July.

54